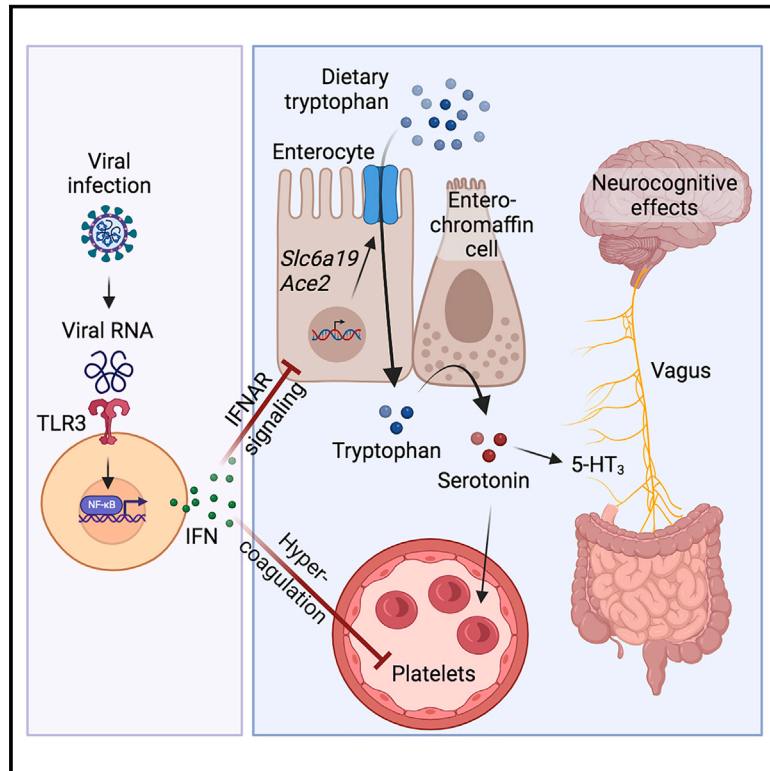


Serotonin reduction in post-acute sequelae of viral infection

Graphical abstract



Authors

Andrea C. Wong, Ashwarya S. Devason, Iboro C. Umana, ..., Sara Cherry, Christoph A. Thaiss, Maayan Levy

Correspondence

benjamin.abramoff@penmedicine.upenn.edu (B.A.A.),
cherrys@penmedicine.upenn.edu (S.C.),
thaiss@penmedicine.upenn.edu (C.A.T.),
maayanle@penmedicine.upenn.edu (M.L.)

In brief

Post-viral syndromes are associated with serotonin reduction, which may contribute to the neurological and cognitive symptoms seen in individuals with Long COVID.

Highlights

- Long COVID is associated with reduced circulating serotonin levels
- Serotonin depletion is driven by viral RNA-induced type I interferons (IFNs)
- IFNs reduce serotonin through diminished tryptophan uptake and hypercoagulability
- Peripheral serotonin deficiency impairs cognition via reduced vagal signaling

Article

Serotonin reduction in post-acute sequelae of viral infection

Andrea C. Wong,^{1,2} Ashwarya S. Devason,^{1,2,3} Ibora C. Umana,^{1,2,3} Timothy O. Cox,^{1,2,3} Lenka Dohnalová,^{1,2,3,4} Lev Litichevskiy,^{1,2,3} Jonathan Perla,^{1,2} Patrick Lundgren,^{1,2,3} Zienab Etwebi,⁵ Luke T. Izzo,^{6,7} Jihee Kim,^{1,2,3} Monika Tetlak,^{1,2,3} Hélène C. Descamps,^{1,2,3} Simone L. Park,^{2,8} Stephen Wisser,^{1,2,3} Aaron D. McKnight,^{1,2,3} Ryan D. Pardy,⁹ Junwon Kim,^{1,2,3} Niklas Blank,^{1,2,3} Shaan Patel,^{1,2,3} Katharina Thum,^{1,2,3} Sydney Mason,^{1,2,3} Jean-Christophe Beltra,^{2,8,10} Michaël F. Michieletto,^{2,5,11} Shin Foong Ngiow,^{2,8,10} Brittany M. Miller,^{1,2} Megan J. Liou,^{1,2,3} Bhoomi Madhu,^{1,2} Oxana Dmitrieva-Posocco,^{1,2} Alex S. Huber,⁵ Peter Hewins,¹ Christopher Petucci,¹² Candice P. Chu,⁹ Gwen Baraniecki-Zwil,¹³ Leila B. Giron,¹⁴ Amy E. Baxter,^{2,8} Allison R. Greenplate,^{2,8} Charlotte Kearns,⁵ Kathleen Montone,⁵ Leslie A. Litzky,⁵ Michael Feldman,⁵ Jorge Henao-Mejia,^{2,5,11} Boris Striepen,⁹ Holly Ramage,¹⁵ Kellie A. Jurado,¹ Kathryn E. Wellen,^{6,7} Una O'Doherty,⁵ Mohamed Abdel-Mohsen,¹⁴ Alan L. Landay,¹⁶ Ali Keshavarzian,^{16,17} Timothy J. Henrich,¹⁸ Steven G. Deeks,¹⁹ Michael J. Peluso,¹⁹ Nuala J. Meyer,²⁰ E. John Wherry,^{2,7,8,10} Benjamin A. Abramoff,^{13,*} Sara Cherry,^{2,5,*} Christoph A. Thaiss,^{1,2,3,*} and Maayan Levy^{1,2,7,21,*}

¹Department of Microbiology, Perelman School of Medicine, University of Pennsylvania, Philadelphia, PA, USA

²Institute for Immunology and Immune Health, University of Pennsylvania School of Medicine, Philadelphia, PA, USA

³Institute for Obesity, Diabetes and Metabolism, Perelman School of Medicine, University of Pennsylvania, Philadelphia, PA, USA

⁴Institute for Molecular Bio Science, Goethe University Frankfurt, Frankfurt am Main, Germany

⁵Department of Pathology and Laboratory Medicine, Perelman School of Medicine, University of Pennsylvania, Philadelphia, PA, USA

⁶Department of Cancer Biology, Perelman School of Medicine, University of Pennsylvania, Philadelphia, PA, USA

⁷Abramson Family Cancer Research Institute, University of Pennsylvania, Philadelphia, PA, USA

⁸Department of Systems Pharmacology and Translational Therapeutics, University of Pennsylvania School of Medicine, Philadelphia, PA, USA

⁹Department of Pathobiology, School of Veterinary Medicine, University of Pennsylvania, Philadelphia, PA, USA

¹⁰Parker Institute for Cancer Immunotherapy, Perelman School of Medicine, University of Pennsylvania, Philadelphia, PA, USA

¹¹Division of Protective Immunity, Department of Pathology and Laboratory Medicine, Children's Hospital of Philadelphia, University of Pennsylvania, Philadelphia, PA 19104, USA

¹²Metabolomics Core, Penn Cardiovascular Institute, University of Pennsylvania, Philadelphia, PA, USA

¹³Department of Physical Medicine and Rehabilitation, Perelman School of Medicine, University of Pennsylvania, Philadelphia, PA, USA

¹⁴The Wistar Institute, Philadelphia, PA, USA

¹⁵Department of Microbiology and Immunology, Sidney Kimmel Medical College, Thomas Jefferson University, Philadelphia, PA, USA

¹⁶Department of Internal Medicine, Rush University Medical Center, Chicago, IL, USA

¹⁷Rush Center for Integrated Microbiome and Chronobiology Research, Chicago, IL, USA

¹⁸Division of Experimental Medicine, University of California, San Francisco, San Francisco, CA, USA

¹⁹Division of HIV, Infectious Diseases, and Global Medicine, Department of Medicine, University of California, San Francisco, San Francisco, CA, USA

²⁰Division of Pulmonary and Critical Care Medicine, Perelman School of Medicine, University of Pennsylvania, Philadelphia, PA, USA

²¹Lead contact

*Correspondence: benjamin.abramoff@penmedicine.upenn.edu (B.A.A.), cherrys@penmedicine.upenn.edu (S.C.), thaiss@penmedicine.upenn.edu (C.A.T.), maayanle@penmedicine.upenn.edu (M.L.)

<https://doi.org/10.1016/j.cell.2023.09.013>

SUMMARY

Post-acute sequelae of COVID-19 (PASC, “Long COVID”) pose a significant global health challenge. The pathophysiology is unknown, and no effective treatments have been found to date. Several hypotheses have been formulated to explain the etiology of PASC, including viral persistence, chronic inflammation, hypercoagulability, and autonomic dysfunction. Here, we propose a mechanism that links all four hypotheses in a single pathway and provides actionable insights for therapeutic interventions. We find that PASC are associated with serotonin reduction. Viral infection and type I interferon-driven inflammation reduce serotonin through three mechanisms: diminished intestinal absorption of the serotonin precursor tryptophan; platelet hyperactivation and thrombocytopenia, which impacts serotonin storage; and enhanced MAO-mediated serotonin turnover. Peripheral serotonin reduction, in turn, impedes the activity of the vagus nerve and thereby impairs hippocampal responses and memory. These findings provide a possible explanation for neurocognitive symptoms associated with viral persistence in Long COVID, which may extend to other post-viral syndromes.

INTRODUCTION

Post-viral syndromes arise in a subset of individuals and can persist for months to years after disease onset.¹ The accompanying symptoms are diverse and often include fatigue, post-exertional malaise, memory loss, and other neurocognitive impairments.² A major post-viral syndrome is “Long COVID,” manifesting as post-acute sequelae of COVID-19 (PASC), which are experienced by a subset of individuals after SARS-CoV-2 infection.³ The molecular etiology of most post-viral syndromes, including Long COVID, remains unclear. Several hypotheses have been proposed to explain the persistence of symptoms, including the presence of a viral reservoir that is not cleared after the initial infection,⁴ chronic inflammation, auto-antibody development, and tissue damage as a result of non-resolving anti-viral responses.¹ Another common feature that has been associated with post-viral syndromes is platelet dysfunction and hypercoagulability.⁵ Finally, Long COVID and other post-viral syndromes have been linked to autonomic nervous system dysfunction.⁶ A deeper understanding of whether these mechanisms occur in different subsets of patients or jointly drive disease persistence is urgently needed.

In this study, we perform a metabolomics investigation and find that serotonin levels are a possible discriminator between recovered individuals and Long COVID patients. Using a combination of human cohort studies, animal models of viral infection, and organoid cultures, we determine that the presence of viral RNA and downstream interferon responses cause a decrease in serotonin. Several mechanisms account for this phenomenon, including diminished uptake of the serotonin precursor tryptophan in the gastrointestinal tract, reduced storage in platelets due to thrombocytopenia, and enhanced turnover by serotonin-metabolizing enzymes. One important consequence of peripheral serotonin deficiency is reduced activity of the vagus nerve, which in turn is associated with hippocampal dysfunction and memory loss. Our findings suggest that many of the current hypotheses for the pathophysiology of PASC might be interconnected and offer actionable therapeutic insights.

RESULTS

PASC can be characterized by serotonin reduction

We began our explorations by defining a consensus metabolomics signature of acute COVID-19. We integrated previously published metabolomics datasets across different cohort studies^{7–11} and ranked the metabolites detected in COVID-19 patients by their degree of deviation from the healthy state (Figures 1A and 1B). Among the metabolites most strongly altered during acute COVID-19 were amino acids and their derivatives (Figure 1B). We thus focused on possible roles for these metabolites in Long COVID. We followed a cohort of 1,540 individuals with PASC at Penn Medicine and performed a systematic symptom analysis based on questionnaire surveys and chart review (Figures 1C and S1A–S1C; Table S1). Dimensionality reduction analysis defined eight subtypes of PASC based on symptom similarity (Figure 1D), categorized by different degrees of initial hospitalization for acute infection, mobility impairment, visceral malaise, cardiorespiratory problems, and neurocognitive symp-

toms (Figures 1D–1F and S1D–S1S). We then performed targeted plasma metabolomics on 58 Long COVID patients who were representative of different clusters (Figure S1T) and experienced persistent symptoms 3 to 22 months after acute infection (Figure S2A). We compared them to 60 individuals with acute COVID-19 and 30 individuals with symptom-free recovery from COVID-19 (Figures 1G and S2B–S2D; Table S2). Notably, the metabolite profile of Long COVID patients was distinct from individuals who recovered to a symptom-free state after SARS-CoV-2 infection (Figure 1H). To determine those molecules that drive the altered metabolomics state in Long COVID, we correlated the abundance of each amino acid metabolite with the presence of symptoms (Figure S2E). We identified a set of molecules whose levels were depleted in both acute and post-acute COVID-19 (Figure 1I), the most significant of which was serotonin (5-hydroxytryptamine, 5-HT) (Figures 1J and S2E). In the post-acute state of infection, serotonin levels were predictive of whether a patient fully recovered or developed long-term sequelae (Figure S2F). Several other amino acids and their derivatives were either unaffected during acute COVID-19 or returned to normal levels in both recovered individuals and Long COVID patients (Figures S2G–S2I).

We sought to verify this finding in other cohorts. In a metabolomics study of Long COVID patients and healthy controls (from Cork, Ireland¹²), serotonin was among the metabolites whose abundance was most strongly depleted in individuals with PASC (Figures S2J–S2L). In contrast, no serotonin reduction was observed in participants of the UNCOVER cohort¹³ (Figures S2M and S2N; Table S3). In this study, patients were enrolled during acute COVID-19 and then longitudinally provided follow-up blood samples and symptom questionnaires.¹³ Conversely, the participants at Penn Medicine were enrolled after seeking treatment at a post-COVID clinic. We thus speculated that the severity of PASC might be greater in a cohort that presents for treatment than in a longitudinal recovery cohort. Indeed, the average number of symptoms was higher in the Penn Medicine cohort compared to UNCOVER (Figure S2O). To corroborate whether different levels of circulating serotonin can be explained by differences in PASC symptoms, we measured plasma serotonin levels in a separate longitudinal study (UCSF LIINC cohort¹⁴), which includes individuals with a wide range of symptoms (Figure S2P; Table S4). Indeed, in this cohort, serotonin levels negatively correlated with the number of symptoms that participants reported three to four months after acute infection (Figure S2Q). Serotonin levels during the acute phase of SARS-CoV-2 infection were not predictive of the development of PASC (Figures S2R and S2S). Taken together, these investigations reveal that serotonin levels are diminished during acute COVID-19 and remain reduced in severe cases of PASC.

Viral inflammation decreases plasma serotonin levels

Given the centrality of serotonin in regulating a large array of physiological processes,¹⁵ we investigated the mechanisms underlying its decrease during acute infection and Long COVID. We first explored whether serotonin depletion was unique to COVID-19 or whether other acute viral infections led to a similar decrease. To this end, we measured serotonin levels in the

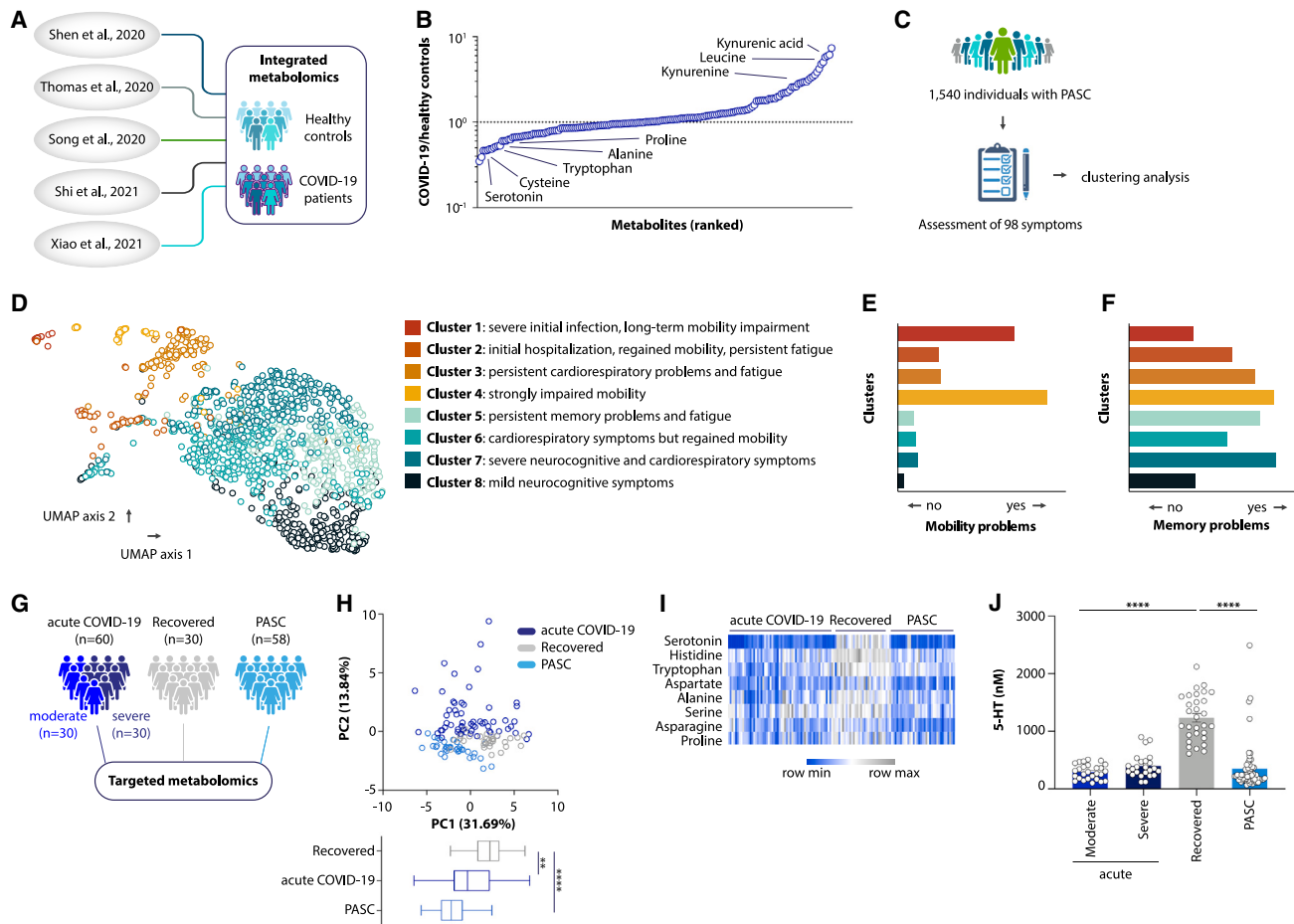


Figure 1. Serotonin deficiency in PASC

(A and B) Study schematic (A) and differential abundance ranking (B) of metabolomics data from COVID-19 patients vs. healthy controls. (C and D) Study schematic (C) and uniform manifold approximation and projection (UMAP) clusters (D) of symptom presentation in UPenn PASC cohort. (E and F) Symptom distribution in PASC cohort clusters. (G–J) Study schematic (G), principal component analysis (PCA) plot and PC1 values from targeted metabolomics data (H), heatmap of metabolites decreasing in acute COVID-19 and not recovering in PASC (I), and plasma serotonin (J) in acute COVID-19, recovered, and PASC patients. Plotted are means \pm SEM. **p < 0.01, ****p < 0.0001. See also [Figures S1](#) and [S2](#).

plasma of 33 individuals with non-SARS-CoV-2 systemic viral infections and compared them to 20 healthy controls ([Figures 2A](#) and [S3A–S3D](#); [Tables S5](#) and [S6](#)). As in acute COVID-19, serotonin levels were strongly decreased by other viral infections ([Figure 2B](#)), suggesting that this might be a more general characteristic of systemic viral infection.

To investigate the mechanisms underlying this association, we used mouse models of viral infection. We first infected mice expressing human ACE2 (K18-ACE2) with the ancestral strain of SARS-CoV-2 ([Figures 2C](#) and [2D](#)). Notably, SARS-CoV-2 infection of K18-ACE2 mice led to a reduction in circulating serotonin ([Figure 2E](#)). We also observed reduced serotonin in wild-type mice infected with the beta variant of SARS-CoV-2¹⁶ ([Figures 2C](#), [2F](#), and [2G](#)). Consistent with our human cohorts, this was not a unique property of SARS-CoV-2, since infection of mice with vesicular stomatitis virus (VSV) similarly decreased plasma serotonin levels ([Figures 2C](#), [2H](#), and [2I](#)).

Several studies indicate that viral persistence might be a characteristic feature of PASC.^{17–21} We addressed this question using the lymphocytic choriomeningitis virus (LCMV) mouse model of persistent viral infection ([Figure 2C](#)). While serotonin levels returned to baseline after clearance of an acute infection (LCMV Armstrong), chronic viral infection sustained serotonin reduction (LCMV clone 13) ([Figures 2J](#), [2K](#), and [S3E–S3H](#)). We thus speculated that reduced serotonin levels in Long COVID might be a consequence of unresolved inflammation induced by viral products. To test this, we recreated viral-induced inflammation in the absence of a replicating pathogen by repeatedly injecting mice with the synthetic double-stranded RNA polyinosinic:polycytidylic acid (poly(I:C)), which mimics viral replication intermediates. Notably, poly(I:C) treatment was sufficient to diminish serotonin levels ([Figures 2L](#) and [S3I](#)) both in total plasma and in isolated platelets, which are the major reservoir of circulating serotonin ([Figures S3J](#) and [S3K](#)). This effect was reversible since

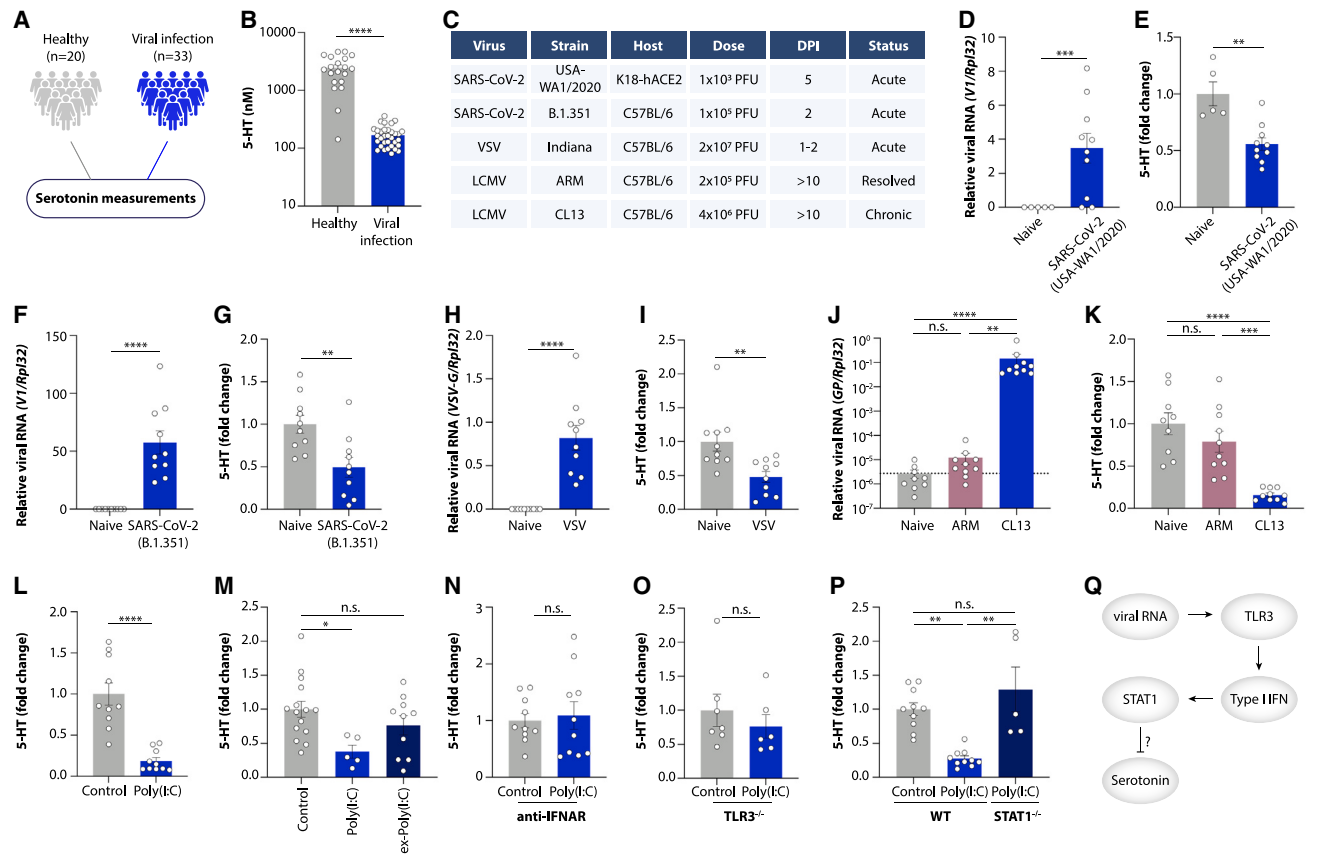


Figure 2. Viral inflammation drives serotonin deficiency

(A and B) Study schematic (A) and plasma serotonin (B) in viremia patients vs. healthy controls.

(C) Overview of viral infections in mice.

(D and E) Viral RNA load in lungs (D) and plasma serotonin levels (E) in K18-hACE2 mice infected with SARS-CoV-2 (USA-WA 1/2020).

(F and G) Viral RNA load in lungs (F) and plasma serotonin levels (G) in mice infected with SARS-CoV-2 (B.1.351).

(H and I) Viral RNA load in spleen (H) and plasma serotonin levels (I) in mice infected with VSV.

(J and K) Viral RNA load in ileum (J) and plasma serotonin levels (K) in mice infected with LCMV Armstrong (ARM) or Clone 13 (CL13) for 15 days.

(L–P) Plasma serotonin levels in control and poly(I:C)-treated mice (L and M), ex-poly(I:C) mice (M), anti-IFNAR-treated mice (N), TLR3^{-/-} mice (O), and STAT1^{-/-} mice (P).

(Q) Schematic of serotonin reduction by viral RNA.

Plotted are means ± SEM. n.s. $p > 0.05$, * $p < 0.05$, ** $p < 0.01$, *** $p < 0.001$, **** $p < 0.0001$. See also Figure S3.

normal serotonin levels were restored within a week of poly(I:C) cessation (Figure 2M).

Both viral infection and poly(I:C) treatment induce type I interferon (IFN) signaling. Indeed, exposure to SARS-CoV-2, infection with VSV, persistence of LCMV, or injection of poly(I:C) all strongly upregulated the levels of interferon-stimulated genes (ISGs; Figures S3L–S3O). Importantly, sustained elevation of type I interferons has been observed in Long COVID patients.²² We therefore asked whether the interferon response caused serotonin reduction. Inhibiting interferon signaling through the interferon alpha receptor (IFNAR) prevented poly(I:C)-induced serotonin reduction (Figure 2N). Moreover, mice with genetic deficiency in either the poly(I:C) receptor TLR3 or in the ISG-inducing transcription factor STAT1 (Figures S3P and S3Q) were resistant to the effects of poly(I:C) on serotonin levels (Figures 2O and 2P). Serotonin depletion did not appear to contribute to host defense, since pharmacological inhibition of

the serotonin-synthesizing enzyme TPH1 enhanced viral loads and pathogenesis during VSV infection and had no effect on SARS-CoV-2 replication (Figures S3R–S3V). Collectively, these findings suggest that the canonical pathway of viral RNA sensing and type I interferon induction by TLR3 leads to serotonin depletion (Figure 2Q).

Viral inflammation blocks intestinal tryptophan uptake

We next investigated the mechanisms by which viral-induced inflammation reduces serotonin levels. The large majority of circulating serotonin is produced in the gastrointestinal tract, where it is synthesized from dietary tryptophan in enterochromaffin cells²³ (Figure 3A). We thus investigated whether serotonin production during viral infection might be limited by reduced tryptophan availability. Indeed, individuals with acute COVID-19 showed reduced plasma tryptophan levels (Figures 1B and 3B).^{24–26} Moreover, tryptophan levels were decreased in Long

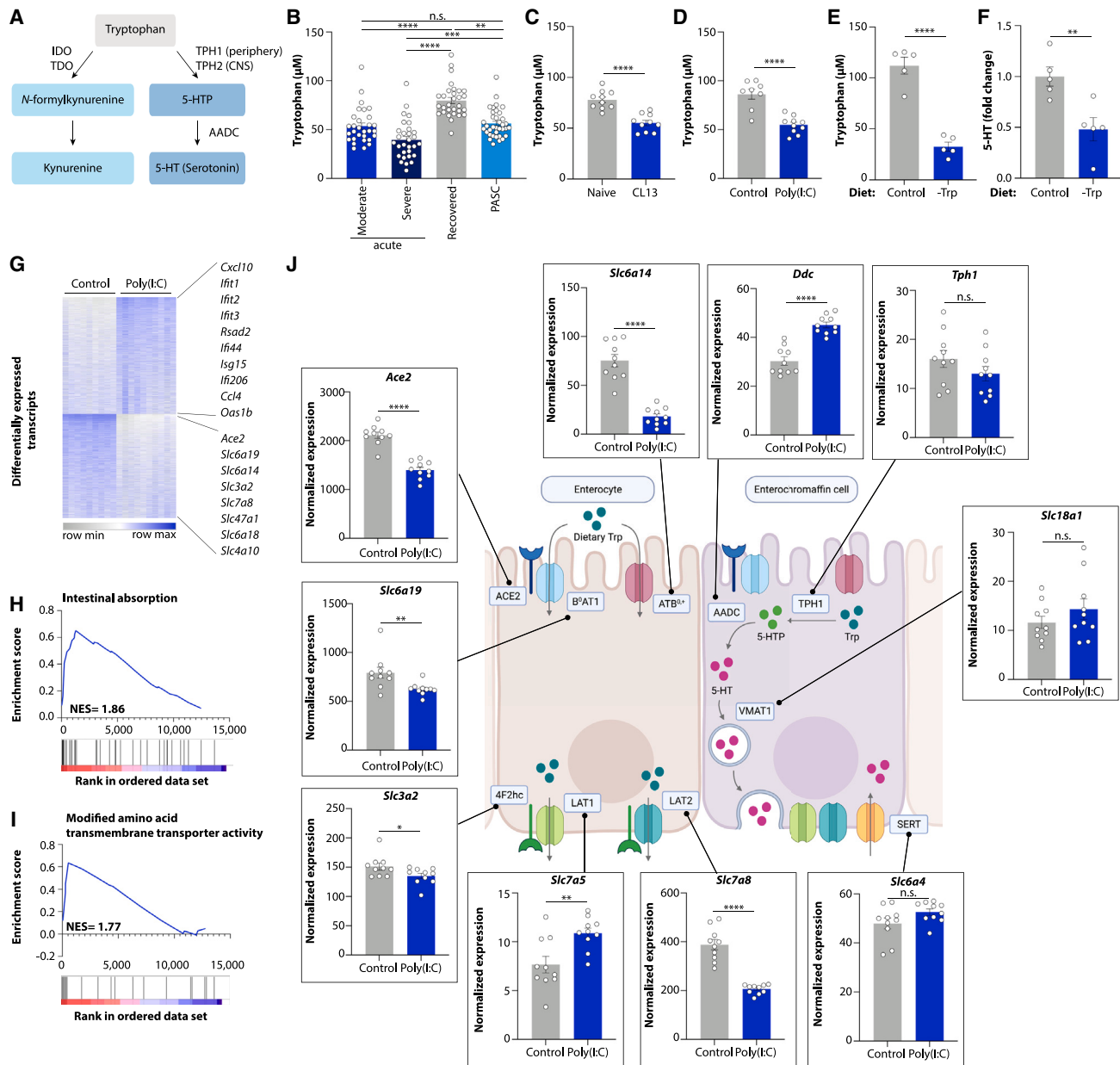


Figure 3. Viral inflammation suppresses genes involved in intestinal amino acid absorption

(A) Schematic of kynurenine and serotonin biosynthesis.

(B–F) Plasma levels of tryptophan (B–E) and serotonin (F) in acute COVID-19, recovered, and PASC patients (B), mice infected with LCMV CLM13 for 30 days (C), poly(I:C)-treated mice (D), and mice fed a tryptophan-deficient diet (E and F).

(G) Differentially expressed genes in ileum of poly(I:C)-treated mice vs. controls.

(H and I) Gene set enrichment analysis plots of ileal genes downregulated by poly(I:C) treatment.

(J) Ileal expression of genes involved in tryptophan uptake and serotonin biosynthesis.

Plotted are means \pm SEM. n.s. $p > 0.05$, * $p < 0.05$, ** $p < 0.01$, *** $p < 0.001$, **** $p < 0.0001$. See also Figure S4.

COVID patients (Figures 1B and 3B). A similar decrease in tryptophan levels was observed in the UCSF LIINC cohort and in another independent Long COVID study (Rush University) (Figures S4A and S4B; Table S4). Plasma tryptophan concentrations were likewise reduced during chronic LCMV infection and after poly(I:C) treatment of mice (Figures 3C and 3D), suggesting

that lower tryptophan availability may cause serotonin reduction by substrate limitation. Consistently, feeding a tryptophan-deficient diet to mice phenocopied the effect of poly(I:C) treatment on plasma serotonin levels in mice (Figures 3E and 3F).

Generally, tryptophan deficiency can be caused by either reduced intestinal absorption or by enhanced conversion into

tryptophan derivatives such as kynurenine (Figure 3A). Kynurenine levels are elevated during viral infection, and numerous reports have highlighted kynurenine as a metabolite strongly induced by SARS-CoV-2 infection^{7–11} (Figure 1B). Indeed, kynurenine levels were increased during acute COVID-19 in our cohort (Figure S4C) and likewise elevated by poly(I:C) treatment of mice (Figure S4D). We therefore hypothesized that serotonin reduction was a consequence of tryptophan depletion due to increased kynurenine production. However, the increase in kynurenine levels did not persist in individuals with PASC (Figure S4C). Furthermore, mice lacking the kynurenine-producing enzyme IDO1, which are deficient in kynurenine production, still presented with reduced serotonin upon poly(I:C) treatment (Figures S4E and S4F). Similarly, pharmacological inhibition of the alternative kynurenine-producing enzyme TDO2 did not restore serotonin levels (Figures S4G and S4H). These findings make it unlikely that kynurenine production is the major cause for serotonin depletion during viral inflammation.

We therefore explored intestinal amino acid uptake as a possible cause of tryptophan deficiency and serotonin depletion. Since poly(I:C) treatment reduces food intake (Figure S4I),^{28,29} we speculated that tryptophan deficiency may result from diminished consumption of this essential amino acid. However, the poly(I:C)-induced tryptophan and serotonin reduction was seen even after an extended fast, in paired feeding experiments, and in experiments in which we supplemented food to poly(I:C)-injected mice (Figures S4J–S4N). The number of serotonin-producing enterochromaffin cells was unaltered by poly(I:C) treatment, ruling out enzymatic synthesis of serotonin as the critical bottleneck (Figures S4O and S4P). We thus used an unbiased approach to explore the impact of viral inflammation on intestinal nutrient absorption. We performed RNA-sequencing of small intestinal tissue of poly(I:C)-treated mice and controls, which revealed strong alterations in intestinal gene expression (Figure S4Q). Expectedly, most upregulated genes belonged to viral recognition and inflammation pathways (Figures 3G and S4R). Remarkably, the gene functions most significantly diminished by poly(I:C) treatment were involved in nutrient metabolism, including amino acid absorption (Figures 3G–3I, S4R, and S4S). For example, the expression of the apical global amino acid transporter $ATB^{0,+}$ (*Slc6a14*), the neutral amino acid transporter B^0AT1 (*Slc6a19*), and the B^0AT1 chaperone ACE2 were all strongly decreased in poly(I:C)-treated mice (Figures 3G and 3J). The expression of transporters on the basolateral side, such as LAT2 (*Slc7a8*), were likewise reduced (Figures 3G and 3J). In contrast, the biosynthetic pathway converting tryptophan into serotonin, including the rate-limiting enzyme TPH1, was not affected (Figure 3J). These data highlight transcriptional downregulation of key amino acid absorption genes during viral inflammation, which we verified by qPCR of intestinal tissue from poly(I:C)-treated mice (Figures S5A–S5K).

We next used both mice and intestinal organoids to reconstruct the poly(I:C)-induced signaling pathway leading to transcriptional alteration in tryptophan uptake genes (Figures S5A and S5L). As in intestinal tissue, small intestinal organoids responded to poly(I:C) with downregulation of *Ace2* and *Slc6a19* (Figures 4A, 4B, and S5M). TLR3 deletion prevented the downregulation of these genes after poly(I:C) injection (Figures 4C and

4D). Inhibition of the transcription factor NF- κ B, which signals downstream to TLR3, blunted the induction of an interferon response and the downregulation of *Ace2* and *Slc6a19* in organoids (Figures 4E, 4F, S5N, and S5O). Notably, exposure to type I interferons was sufficient to reduce the expression of genes involved in tryptophan absorption (Figures 4G, 4H, and S5P). The interferon receptor signals via STAT1, and we verified marked STAT1 phosphorylation in response to poly(I:C) treatment in both organoids and intestinal epithelial cells (Figures S5Q and S5R). STAT1 was required for the transcriptional inhibition of *Ace2* and *Slc6a19* (Figures 4I and 4J) in an epithelial-intrinsic manner (Figures 4K and 4L).

To explore the connection between viral persistence in the gut and transcriptional regulation of tryptophan uptake genes, we examined gastrointestinal samples from both mice and humans after viral infection. Indeed, we observed downregulation of *Ace2* and *Slc6a19* in both acute (VSV) and chronic (LCMV clone 13) settings of viral infection (Figures 4M–4P). Acute SARS-CoV-2 infection in mice also resulted in detectable viral RNA in intestinal tissue (Figures 4Q and 4R), and data from SARS-CoV-2-infected human intestinal organoids³⁰ revealed strong transcriptional inhibition of *ACE2* and *SLC6A19* (Figures 4S and 4T). Numerous reports have suggested that SARS-CoV-2 can replicate in the human gastrointestinal tract and remain detected long after the acute infection.^{17,30,31} We confirmed these findings in tissue samples obtained from autopsies during the acute (<2 weeks) and post-acute (>2 weeks) phase after SARS-CoV-2 infection (Figure 4U). While viral RNA could be amplified from several organs during the acute phase (Figure 4V), the gastrointestinal tract stayed viral-RNA-positive in samples obtained from the post-acute phase (Figures 4V and S5S). To determine whether viral persistence in the gastrointestinal tract was associated with the development of PASC, we collected stool samples from individuals with PASC as well as a control group of individuals with prior SARS-CoV-2 infection but no persistent symptoms (Figure 4U). Viral RNA was indeed detected in the stool of a subset of individuals with PASC (Figure 4W), highlighting a possible connection between the presence of viral components in the gastrointestinal tract and the persistence of long-term symptoms in certain individuals.

We next assessed the consequences of reduced epithelial expression of amino acid uptake genes during viral inflammation. In addition to tryptophan, we noted a pronounced reduction in the plasma concentrations of several amino acids in mice injected with poly(I:C), particularly in neutral amino acids (Figure 5A). This amino acid profile resembled the one in mice lacking ACE2 (Figure 5B), which together with B^0AT1 is required for the transport of neutral amino acids across the apical membrane of intestinal epithelial cells.³² We confirmed that the successive loss of functional *Ace2* alleles in heterozygous and homozygous *Ace2*-deficient mice led to a stepwise reduction in tryptophan levels (Figure 5C). Mice lacking ACE2 were also unable to absorb an oral bolus of tryptophan (Figure 5D), in line with previous findings.³² Notably, the same phenomenon was observed with poly(I:C) treatment of heterozygous *Ace2*-deficient mice (Figure 5E), indicating that transcriptional downregulation of *Ace2* in these mice phenocopied the homozygous *Ace2*-deficient state. While the systemic levels of tryptophan were reduced, ileal

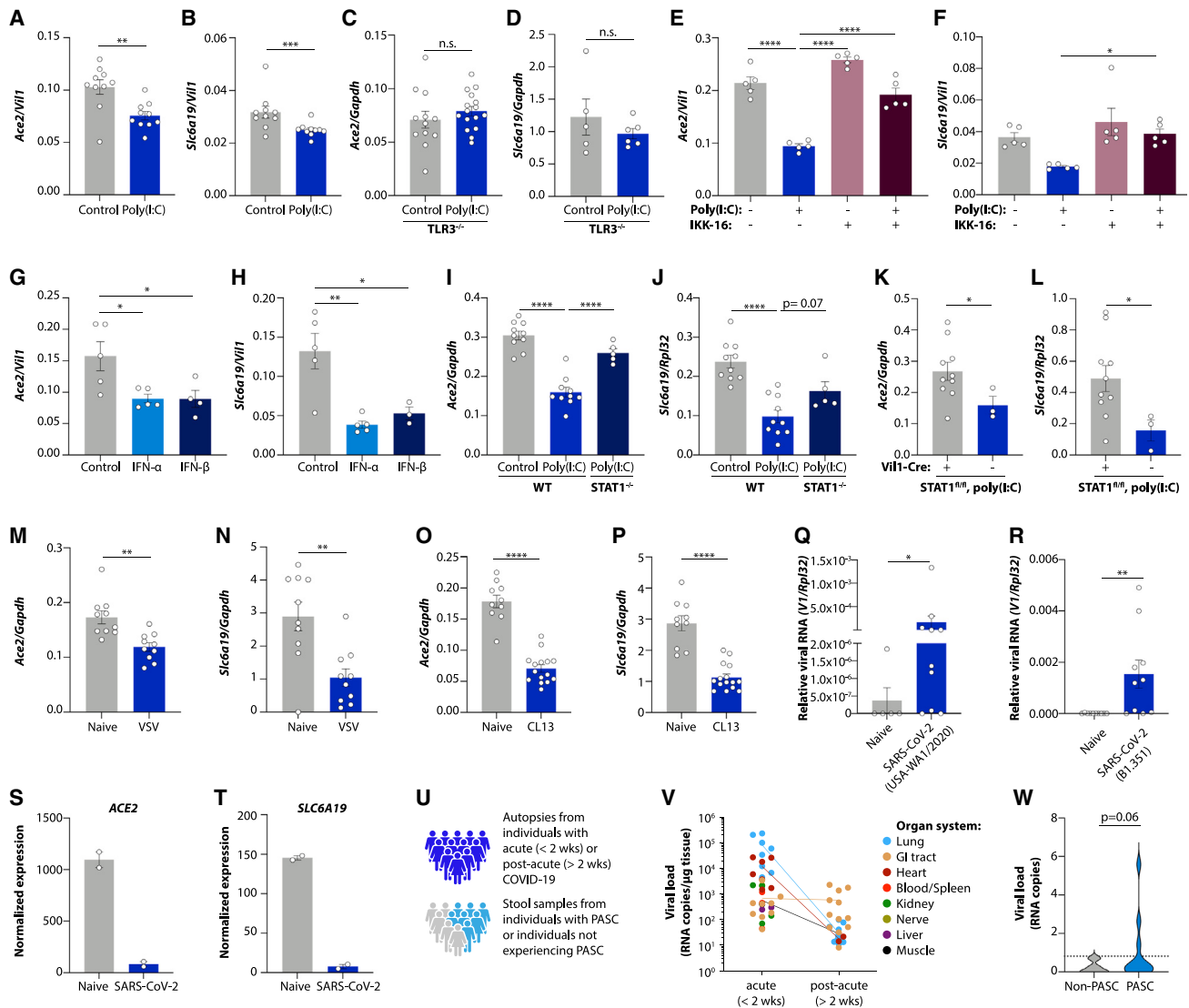


Figure 4. Mechanisms of viral inflammation-induced intestinal gene expression changes

(A–P) *Ace2* and *Slc6a19* expression in poly(I:C)-treated small intestinal organoids (A and B), poly(I:C)-treated TLR3^{-/-} mice (C and D), poly(I:C) and IKK-16-treated small intestinal organoids (E and F), IFN- α - and IFN- β -treated small intestinal organoids (G and H), poly(I:C)-treated STAT1^{-/-} mice (I and J), poly(I:C)-treated Villin^{Cre-ERT2/+} STAT1^{fllox/fllox} mice (K and L), ileum of VSV-infected mice (M and N), and ileum of LCMV CL13-infected mice 27 days post-infection (O and P). (Q and R) Intestinal viral RNA after infection with the indicated strains of SARS-CoV-2.

(S and T) Normalized expression of *Ace2* (S) and *Slc6a19* (T) in SARS-CoV-2-infected human small intestinal organoids.³⁰

(U–W) Study schematic (U), SARS-CoV-2 RNA detected in tissues obtained from autopsies during the acute or post-acute phase after infection (V), and SARS-CoV-2 RNA detected in stool obtained from individuals with PASC and a control group of individuals with prior SARS-CoV-2 infection but no persistent symptoms (W).

Plotted are means \pm SEM. n.s. $p > 0.05$, * $p < 0.05$, ** $p < 0.01$, *** $p < 0.001$, **** $p < 0.0001$. See also Figure S5.

tryptophan accumulated after poly(I:C) injection (Figures 5F and 5G). Isotope tracing confirmed that circulating tryptophan is derived from the orally supplemented source (Figure S6A), highlighting that poly(I:C) treatment prevented tryptophan absorption.

If tryptophan uptake was abrogated by poly(I:C) treatment, tryptophan supplementation should elevate serotonin levels even during viral inflammation. To corroborate this, we used

a diet containing a glycine-tryptophan dipeptide, which bypasses the need for B⁰AT1 and enables tryptophan uptake via dipeptide transporters.³³ This diet compensated for impaired uptake in poly(I:C)-treated mice and led to an increase in both tryptophan and serotonin levels in systemic circulation (Figures 5H and 5I). Similarly, supplementation with the serotonin precursor 5-hydroxytryptophan (5-HTP), which bypasses the requirement for tryptophan, rescued serotonin

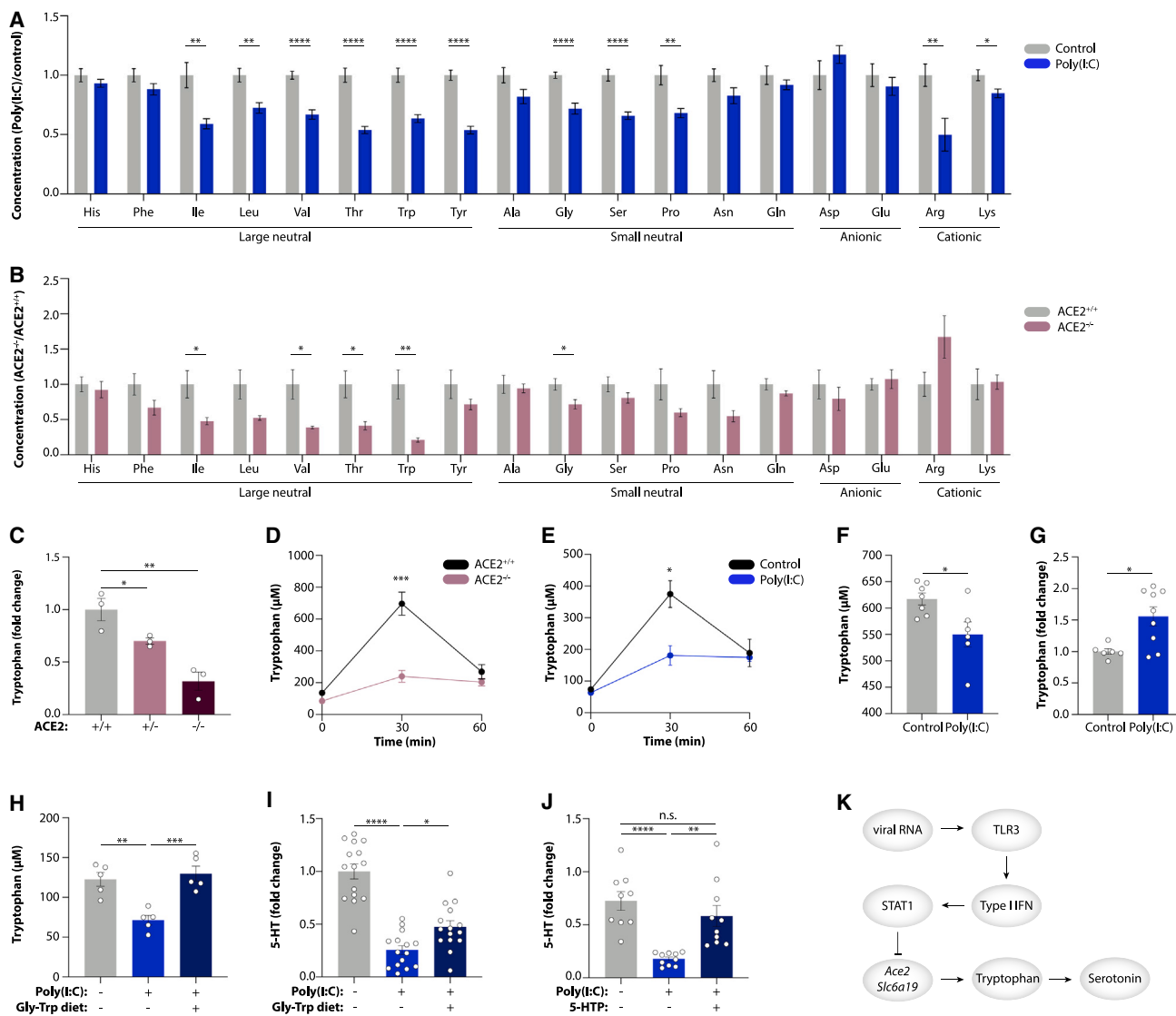


Figure 5. Viral inflammation inhibits intestinal amino acid absorption

(A and B) Targeted plasma metabolomics in poly(I:C)-treated mice vs. controls (A) and ACE2^{-/-} vs. ACE2^{+/+} mice (B).

(C) Plasma tryptophan in ACE2^{+/+}, ACE2^{+/-}, and ACE2^{-/-} mice.

(D and E) Plasma tryptophan in ACE2^{+/+} vs. ACE2^{-/-} mice (D) and poly(I:C)-treated mice vs. controls (E) after tryptophan gavage.

(F and G) Tryptophan levels in sera (F) and ileal content (G) of poly(I:C)-treated mice 30 min following tryptophan gavage.

(H–J) Plasma tryptophan (H) and serotonin (I and J) in poly(I:C)-treated mice fed a Gly-Trp dipeptide diet (H and I) or given the serotonin precursor 5-HTP (J).

(K) Schematic of serotonin reduction by viral RNA via reduced tryptophan uptake.

Plotted are means ± SEM. n.s. p > 0.05, *p < 0.05, **p < 0.01, ***p < 0.001, ****p < 0.0001. See also Figure S6.

levels in poly(I:C)-injected mice (Figure 5J). Collectively, these data demonstrate that viral-RNA-induced inflammation impairs intestinal tryptophan uptake, which causes systemic serotonin depletion (Figure 5K).

Viral inflammation impairs serotonin storage

Upon synthesis in enterochromaffin cells, circulating serotonin is transported inside platelets, while free serotonin is rapidly degraded by monoamine oxidase (MAO) enzymes (Figure 6A).³⁴ We noted that platelet counts were strongly decreased after

acute VSV infection, chronic LCMV infection, and poly(I:C) injection,³⁵ providing a possible explanation for reduced circulating serotonin levels (Figures 6B–6D). Poly(I:C)-induced thrombocytopenia was dependent on the TLR3-IFN-STAT1 signaling pathway (Figures 6E–6G). The overall white blood cell count was unchanged by poly(I:C) treatment (Figure S6B). Erythrocyte, hemoglobin, and hematocrit counts were reduced (Figures S6C–S6E), while mean corpuscular volume and mean corpuscular hemoglobin were not affected (Figures S6F and S6G). Increased mean platelet volumes (Figures 6H and 6I) were indicative of

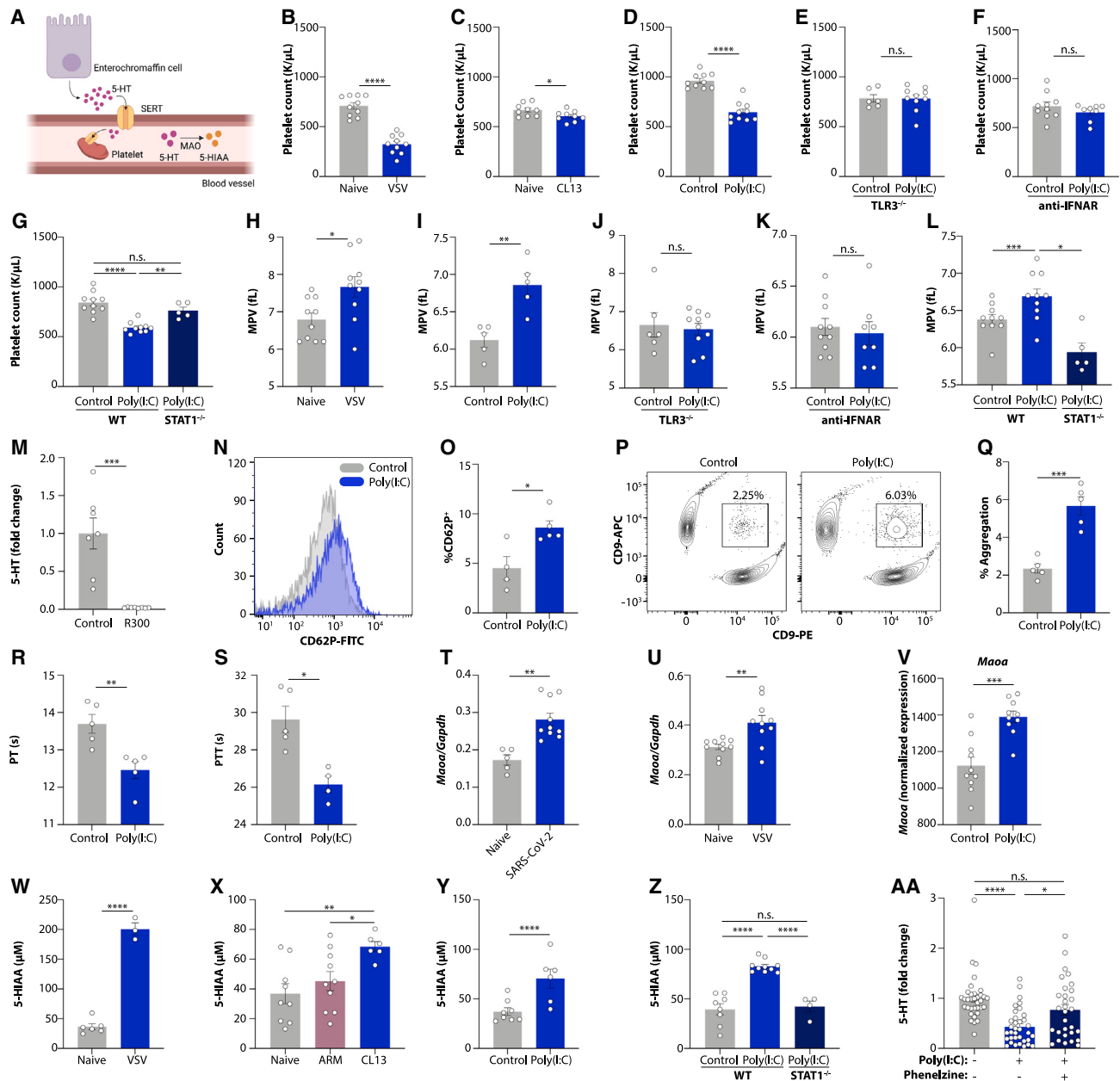


Figure 6. Viral inflammation drives thrombocytopenia and serotonin turnover

(A) Cartoon of serotonin transport and degradation.

(B–G) Platelet counts in naive or VSV-infected mice (B); LCMV CL13-infected mice at day 15 post-infection (C); and poly(I:C)-treated wild-type (D), TLR3^{-/-} (E), anti-IFNAR-receiving (F), and STAT1^{-/-} mice.

(H–L) Mean platelet volume of VSV-infected mice (H) and poly(I:C)-treated wild-type (I), TLR3^{-/-} (J), anti-IFNAR-receiving (K), and STAT1^{-/-} mice (L).

(M) Plasma serotonin in mice treated with a platelet-depleting antibody.

(N–Q) Representative FACS plot (N and P) and quantification (O and Q) of platelet CD62P expression (N and O) and platelet aggregation (P and Q) in poly(I:C)-treated mice.

(R and S) Prothrombin (R) and partial thromboplastin (S) time in poly(I:C)-treated mice.

(T–V) Ileal *Maaol* expression in mice treated with SARS-CoV-2 (USA-WA 1/2020) (T), VSV (U), or poly(I:C) (V).

(W–Z) 5-HIAA levels in urine from mice infected with VSV (W) and LCMV ARM or CL13 at day 15 post-infection (X), as well as poly(I:C)-treated wild-type (Y) and STAT1^{-/-} mice (Z).

(AA) Platelet serotonin levels of poly(I:C)-treated mice receiving the MAO inhibitor phenelzine.

Plotted are means ± SEM. n.s. p > 0.05, *p < 0.05, **p < 0.01, ***p < 0.001, ****p < 0.0001. See also Figure S6.

increased destruction of platelets,^{36–40} which was likewise dependent on TLR3, type I interferon signaling, and STAT1 (Figures 6J–6L). Tryptophan supplementation was unable to restore platelet counts (Figure S6H), indicating that reduced intestinal amino acid uptake and platelet depletion were independent effects of poly(I:C) injection. Consistently, platelet depletion⁴¹ abolished circulating serotonin levels (Figures 6M and S6I) without affecting intestinal tryptophan uptake genes (Figures S6J and S6K).

We next investigated the causes for thrombocytopenia during viral inflammation. The number and size of megakaryocytes in the bone marrow was increased in poly(I:C)-treated mice (Figures S6L–S6N), while thrombopoietin levels were unchanged (Figures S6O and S6P). We noted that the baseline activation status of platelets was increased by poly(I:C) treatment (Figures 6N and 6O). Consistently, platelet aggregation was markedly enhanced (Figures 6P and 6Q). Prothrombin time (PT) and partial thromboplastin time (PTT) were reduced (Figures 6R and 6S), further indicative of hypercoagulability.⁴² We ruled out changes in the concentrations of fibrinogen, tissue factor, or TAT complexes as alternative explanations (Figures S6Q–S6S). Collectively, these results indicate that viral inflammation drives platelet hyperactivation, resulting in hypercoagulability and thrombocytopenia in an interferon-dependent manner. Consequently, platelet-mediated systemic serotonin transport is impaired.

Since free serotonin is the target of rapid degradation,³⁴ we next focused on MAO-mediated serotonin turnover. We found that intestinal transcript levels of *Maoa* were increased in SARS-CoV-2-infected, VSV-infected, and poly(I:C)-treated mice in a TLR3-dependent manner (Figures 6T–6V and S6T). Consistently, the levels of the serotonin degradation product 5-hydroxyindoleacetic acid (5-HIAA) were increased in the urine of virally infected mice and in mice injected with poly(I:C) (Figures 6W–6Y and S6U). STAT1-deficient mice were protected from the accumulation of 5-HIAA (Figure 6Z). Notably, pharmacological inhibition of MAO prevented the accumulation of 5-HIAA and restored serotonin levels in poly(I:C)-treated mice (Figures 6AA and S6V). These findings indicate that serotonin turnover is enhanced during viral inflammation.

Serotonin reduction impairs vagal signaling and memory function

Finally, we explored the consequences of peripheral serotonin depletion on individuals experiencing PASC. In a symptom questionnaire administered at the time of blood draw, the majority of patients in our cohort reported fatigue, cognitive difficulties, headaches, loss of endurance, problems with sleep, anxiety, and memory loss (Figure S7A). To investigate possible mechanisms underlying the association between serotonin reduction and prevalent neurocognitive manifestations, we again turned to mouse models. We observed cognitive impairment in the setting of acute VSV infection, chronic LCMV persistence, and in poly(I:C)-treated mice as assessed by the novel object recognition paradigm⁴³ (Figures 7A–7C). This was dependent on TLR3 and type I interferon signaling^{44,45} (Figures 7D and 7E). Platelet depletion similarly impaired memory function (Figure 7F). We therefore hypothesized that serotonin reduction may be respon-

sible for poor cognitive performance after poly(I:C) injection. Indeed, treatment of mice with the selective serotonin reuptake inhibitor (SSRI) fluoxetine restored novel object recognition (Figure 7G), and rescue of tryptophan levels by glycine-tryptophan supplementation reinstated normal cognitive performance in poly(I:C)-treated mice (Figure 7H). Differences in explorative behavior did not affect the results across all of these experiments (Figures S7B–S7H).

The acquisition of short-term memories is driven by the hippocampus,⁴⁶ and studies have described reduced hippocampal activity in COVID-19 patients.^{47,48} We found that hippocampal activation in response to novel object exposure was blunted in poly(I:C)-treated mice (Figures 7I–7K, S7I, and S7J). This was not accounted for by changes in hippocampal neurogenesis (Figures S7K–S7N). Since serotonin plays an important role in hippocampal function,^{49–51} we hypothesized that serotonin reduction directly impaired the generation of hippocampus-dependent memories. However, serotonin levels in the brain were unaffected by viral inflammation (Figure 7L), suggesting that the peripheral reduction of serotonin was responsible for cognitive impairment.

Circulating serotonin does not cross the blood-brain barrier¹⁵ but can influence the brain via afferent sensory neurons.⁵² To explore the impact of peripheral serotonin on sensory neurons, we measured neuronal activation in sensory terminals of the nucleus tractus solitarius (NTS) in the brainstem. Novelty exposure led to an increase in cFos⁺ cells in the NTS, but this response was abrogated upon poly(I:C) treatment (Figures 7M and 7N), suggesting that serotonin depletion causes cognitive impairment through reduced sensory neuron activity. Consistently, restoration of peripheral serotonin levels using 5-HTP rescued cognition in poly(I:C)-treated mice (Figures 7O and S7O), and so did the TRPV1 agonist capsaicin, a strong stimulant of sensory neurons (Figure 7O). Of note, capsaicin treatment did not affect peripheral serotonin levels (Figure S7O), and neither capsaicin nor 5-HTP treatment ameliorated poly(I:C)-induced ISG responses in the brain (Figure S7P), highlighting that restoration of sensory input from the periphery is able to rescue cognition despite serotonin deficiency or ongoing neuroinflammation. Peripheral serotonin reduction alone, as in the case of platelet depletion, did not trigger inflammation in the brain (Figure S7Q).

TRPV1⁺ sensory neurons can be broadly categorized as vagal and spinal cord afferents. To distinguish between both possibilities, we chemogenetically activated Phox2b-expressing neurons, which are restricted to the vagus nerve. Indeed, stimulation of Phox2b neurons during poly(I:C) treatment restored activation of hippocampal neurons and the formation of short-term memories (Figures 7P–7R and S7R). To determine the mechanism by which serotonin influences the activity of vagal neurons, we used an *in vitro* system in which we cultured neurons from nodose ganglia and exposed them to serotonin. Vagal neurons robustly responded to serotonin treatment, as evidenced by rapid calcium influx (Figure 7S), suggesting a possible direct effect of peripheral serotonin on the vagus nerve. Single-cell transcriptomics data⁵² showed high and selective expression of the serotonin receptor 5-HT₃ on vagal neurons (Figure S7S). To determine whether serotonin signaling via 5-HT₃ receptors was

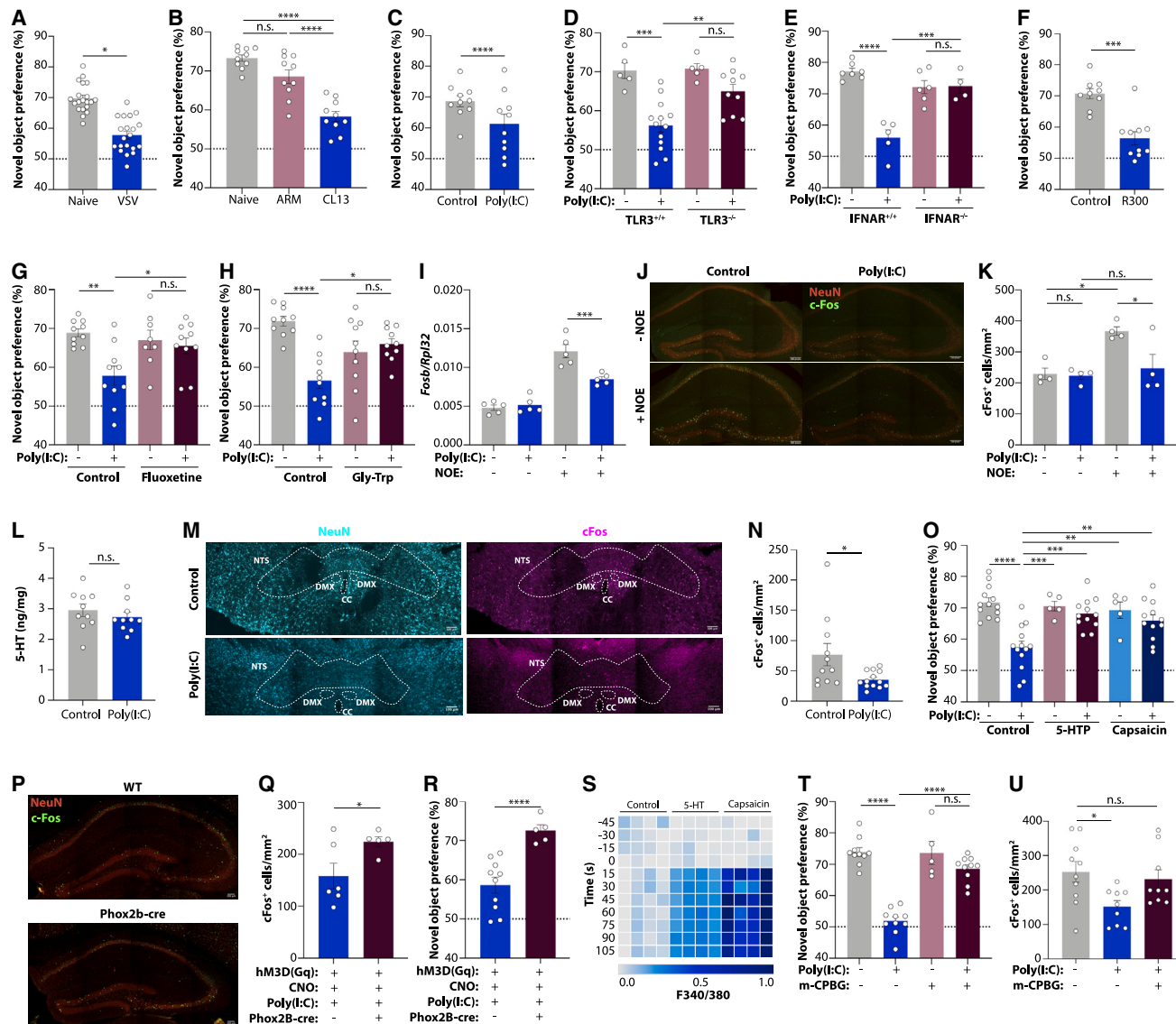


Figure 7. Serotonin deficiency drives cognitive dysfunction via vagal signaling

(A–H) Novel object preference in mice infected with VSV (A) or LCMV ARM or CL13 at day 14 post-infection (B); poly(I:C)-treated wild-type (C), TLR3^{-/-} (D), and IFNAR^{-/-} mice (E); platelet-depleted mice (F); poly(I:C)-treated mice receiving the SSRI fluoxetine (G); and poly(I:C)-treated mice fed a Gly-Trp dipeptide diet (H). (I) Fosb expression in the hippocampus of poly(I:C)-treated mice with or without novel object exposure (NOE). (J and K) Representative images (J) and quantification (K) of cFos⁺ cells in the dentate gyrus of poly(I:C)-treated mice with or without NOE. Scale bars, 100 μ m. (L) Serotonin concentrations in the brains of poly(I:C)-treated mice. (M and N) Representative images (M) and quantification (N) of cFos⁺ cells in the nucleus tractus solitarii (NTS) of poly(I:C)-treated mice. Scale bars, 100 μ m. Outlined are NTS, dorsal motor nucleus (DMX), and central canal (CC). (O) Novel object preference in mice receiving poly(I:C), 5-HTP, or capsaicin. (P–R) Representative images (P) and quantification of cFos⁺ cells in the dentate gyrus following NOE (Q) and novel object preference (R) of Phox2b-cre mice injected with AAV-hM3Dq, CNO, and poly(I:C). Scale bars, 100 μ m. (S) Calcium signaling of cultured vagal neurons exposed to capsaicin or serotonin. (T and U) Novel object preference (T) and quantification of cFos⁺ cells in the dentate gyrus (U) of mice treated with poly(I:C) and the 5-HT₃ receptor agonist m-CPBG.

Plotted are means \pm SEM. n.s. $p > 0.05$, * $p < 0.05$, ** $p < 0.01$, *** $p < 0.001$, **** $p < 0.0001$. See also Figure S7.

sufficient to restore cognition during viral inflammation, we used the pharmacological 5-HT₃ receptor agonist meta-Chlorophenylbiguanide (m-CPBG). Indeed, m-CPBG treatment normalized both novelty responses of hippocampal neurons and perfor-

mance in the novel object recognition paradigm (Figures 7T and 7U). Taken together, these findings suggest that serotonin reduction dampens vagal signaling and thereby impairs cognitive function.

DISCUSSION

The emergence of PASC poses a global health challenge. The pathophysiology of post-viral syndromes remains poorly understood,^{1,3} leaving medical systems across the world unprepared for the large number of individuals developing cardiorespiratory, neurocognitive, gastrointestinal, and musculoskeletal symptoms in the months and years⁵³ following acute COVID-19. While vaccination may reduce the risk of developing PASC,^{54,55} instances of Long COVID after breakthrough infections continue to occur.⁵⁶ A deeper understanding of the molecular and cellular etiopathology of PASC is thus urgently needed.

In this study, we have investigated metabolite signatures associated with Long COVID. We have focused on metabolites whose concentrations are perturbed both in acute COVID-19 and in patients with PASC. Among the metabolites we measured, the molecule most significantly associated with PASC was serotonin. We show that viral inflammation-driven serotonin depletion can be caused by reduction of tryptophan absorption, thrombocytopenia, and increased MAO expression. This response is TLR3-, IFNAR-, and STAT1-dependent and results in decreased vagal and hippocampal activation as well as cognitive impairment.

These findings have several important implications. First, they highlight the profound consequences that persistent viral reservoirs can have. Numerous studies have provided evidence for the presence of viral components^{17–19} and persistently high levels of type I interferons in the blood 8 months after infection.²² Our data indicate that the presence of viral components and resultant interferon response might be a causative factor in the development of PASC-associated symptoms.

Second, our study highlights a mechanism by which viral infection can alter amino acid uptake. Deviations from homeostatic concentrations of amino acids can exert profound effects on tissue function.⁵⁷ While we focused on serotonin in this study, tryptophan serves as the precursor for many other important metabolites, including niacin, NAD, and melatonin.^{23,58} The evolutionary teleology of reduced intestinal amino acid absorption during viral inflammation remains unclear, but it is possible that acute downregulation of genes involved in amino acid uptake is part of a cellular response to interferon stimulation aimed at abrupt cessation of cellular metabolism during viral infection. In the case of non-resolving viral inflammation, this response may persist and result in nutrient deficiency.

Third, a common feature of both acute and post-acute SARS-CoV-2 infection is the formation of microthrombi as a result of hypercoagulability.^{59–61} Our findings imply that thrombocytopenia may diminish the carrying capacity of the systemic circulation for serotonin. Reduced serotonin storage, coupled with the induction of MAO enzymes, may enhance the turnover of serotonin and excretion of its degradation products. Thus, hypercoagulability in acute COVID-19 and Long COVID may have implications beyond its cardiovascular effects.

Fourth, our study indicates a role for the vagus nerve in mediating the impact of serotonin reduction on the brain.⁶² Neurological symptoms are widespread in patients with both acute and post-acute COVID-19.^{63,64} Since unequivocal evidence for SARS-CoV-2 replication in the brain is lacking, recent studies

have focused on the cognitive consequences of peripheral immune activation as well as neuroinflammation.^{63,65} Based on our data, we suggest that afferent sensory neurons may play a critical role in the neurocognitive manifestations of both acute and post-acute viral infections. The vagus nerve is an important mediator of sickness behavior,⁶⁶ responds to peripheral serotonin levels,⁶⁷ and has been implicated in the pathophysiology of chronic fatigue syndrome.⁶⁸ While the precise circuit by which the vagus nerve is involved in the development of PASC remains unclear, sensory neurons may emerge as an important element in relaying the effect of peripheral viral inflammation to the brain.

Finally, our findings indicate possible targets for clinical interventions aimed at the prevention and treatment of PASC. Our animal models demonstrate that serotonin levels can be restored and memory impairment reversed by precursor supplementation or SSRI treatment. While the effectiveness of SSRIs in acute COVID-19 has been a subject of debate,^{69–74} no systematic exploration of SSRIs in individuals with PASC has been performed to date. Our study, together with recent findings linking depression with cognitive impairment in Long COVID⁷⁵ and the effect of SSRIs on vagus nerve activity,⁶⁷ call for the assessment of targeting serotonin signaling for the prevention or treatment of neurocognitive manifestations.

Given the dual role of ACE2 as both a mediator of intestinal tryptophan absorption³² and a receptor for SARS-CoV-2,⁷⁶ it is possible that virus-induced receptor internalization augments the effect of interferons on ACE2 downregulation and serotonin reduction. In principle, however, none of the mechanisms described in this study are unique to SARS-CoV-2 infection. Indeed, reduced serotonin levels have been reported in other settings of viral inflammation, such as dengue virus infection,⁷⁷ which is the trigger of another post-viral syndrome.⁷⁸ The connection between serotonin reduction and vagus nerve dysfunction may thus be relevant beyond Long COVID. The fact that low serotonin levels are also found in non-viral conditions characterized by elevated interferon levels, such as systemic lupus erythematosus or multiple sclerosis,^{79–81} suggests that the pathway described in this study may even apply beyond viral infections.

Limitations of this study

The degree of serotonin reduction is variable across the four cohorts of individuals with PASC that we have examined in this study. While modes of recruitment, number of symptoms, and degree of disease severity might provide possible sources of this variability, there are likely further differences that we have not accounted for. The manifestations of Long COVID are highly heterogeneous,⁸² and the subtypes of PASC that are studied in individual cohorts are likely different. Our results indicate that serotonin reduction is not specific to any particular subset of PASC, but much larger numbers of longitudinal samples are required to comprehensively characterize serum metabolite levels across the different endotypes of Long COVID.

In addition, while we provide evidence for serotonin reduction in acute COVID-19, individuals with PASC, and acutely and chronically infected mice, mouse models for Long COVID are still lacking, and thus our study does not establish a direct causal connection between post-acute SARS-CoV-2 infection,

tryptophan uptake, thrombocytopenia, and serotonin levels. The chronic LCMV and poly(I:C) models used in this study recapitulate important features of SARS-CoV-2 infection but have clear limitations. For instance, when administered systemically, poly(I:C) may not accurately mimic the tissue-level inflammatory processes induced by persistent viral reservoirs. Furthermore, while the persistent presence of circulating spike protein may be a useful marker for PASC,¹⁸ it remains unclear whether remnants of SARS-CoV-2 nucleic acid play any functional role in Long COVID.

Finally, our assessment of viral persistence in the gastrointestinal tract of individuals with PASC is based on a limited number of participants. Similarly, we have not demonstrated a direct connection between intestinal viral persistence and chronically elevated levels of type I interferons in humans, which would require collecting a large number of intestinal biopsies from Long COVID patients. Our results thus call for the large-scale investigation of the causal connection between the presence of a viral reservoir in the gastrointestinal tract, sustained inflammatory responses, and manifestations of Long COVID.

STAR★METHODS

Detailed methods are provided in the online version of this paper and include the following:

- **KEY RESOURCES TABLE**
- **RESOURCE AVAILABILITY**
 - Lead contact
 - Materials availability
 - Data and code availability
- **METHOD DETAILS**
 - Mice
 - Poly(I:C) treatment
 - Novel object recognition test
 - Radiolabeled tryptophan measurements
 - *In vivo* treatments
 - AAV injections
 - Patients, participants, and clinical data collection
 - Quantification of SARS-CoV-2 viral copies in stool samples
 - Organoids
 - Paired food intake and food gavage
 - BioDAQ cages
 - Platelet depletion
 - Platelet aggregation FACS
 - Western blots
 - Nodose ganglion extraction, culture, and calcium imaging
 - Intestinal immunofluorescence
 - Hippocampus and nucleus tractus solitarius (NTS) immunofluorescence
 - Metabolomics
 - VSV infections
 - LCMV infections
 - Diets
 - SARS-CoV-2 mouse infections
 - Tryptophan gavage

- PTT and aPTT
- Flow cytometric assessment of platelet activation
- Hematology analysis
- Megakaryocyte analysis
- Platelet and platelet-rich-plasma isolation
- Metabolite and soluble factor measurements
- BCA protein quantification
- RNA sequencing analysis of human organoids
- Transcriptional profiling by bulk-RNA sequencing
- GSEA analysis
- Single-cell RNA-sequencing analysis
- Quantitative real-time PCR

● QUANTIFICATION AND STATISTICAL ANALYSIS

SUPPLEMENTAL INFORMATION

Supplemental information can be found online at <https://doi.org/10.1016/j.cell.2023.09.013>.

ACKNOWLEDGMENTS

We thank all study participants and acknowledge James Heath (ISB) for providing samples from the INCOV/UNCOVER study. We also acknowledge the following individuals and cores at UPenn for their contributions to this study: Eline Luning Prak (Human Immunology Core), MESSI Cohort Study (supported by grants HL137006 and HL137915), COVID Processing Unit, PennMedicine Biobank, M. Risman, J. Weaver, M. Livingstone, Post-COVID Assessment and Recovery Clinic, Center for Human Phenomic Science, Molecular Pathology and Imaging Core, CDB Microscopy Core Facility, Bates laboratory, Hensley laboratory, Animal Biosafety Level 3 Core, Matthew Lanza (Vet Comparative Pathology Core), Collman laboratory, J. Graham-Wooten, Muzykantov laboratory, Lee laboratory, and R. Hess. The Vet Comparative Pathology Core is supported by the Abramson Cancer Center (P30 CA016520). The Human Immunology Core is supported by the NIH (P30-CA016520 and P30-AI045008), the Department of Pathology and Laboratory Medicine, and the Penn Center for Precision Medicine. We thank E. Krause, K. Scott, and A. de Kloet (University of Florida) for providing mice. We acknowledge grants T32-AI-055400-19 (A.C.W.); F31HL160065 and T32-AI-141393 (P.L.); Boehringer Ingelheim Fonds MD fellowship (Jihee Kim); Canadian Institutes for Health Research and the Fonds de Recherche du Québec - Santé (R.D.P.); Hartwell Foundation (M.J.L.); T32-AI-055400 (B.M.M.); Cancer Research Institute Irvington Postdoctoral Fellowship (S.L.P.); Cancer Immunotherapy Bridge fellowship (J.B.); Australia NHMRC C.J. Martin Fellowship GNT1111469 and Mark Foundation Momentum Fellowship (S.N.); NIH R01 DK123733 (M.A.-M., A.L., and A.K.); and NIH R01AA029859 (A.K. and M.A.-M.). E.J.W. is supported by The Parker Institute for Cancer Immunotherapy; NIH grants AI155577, AI149680, AI108545, AI082630 and CA210944; and the Polybio Research Foundation. M.P. is supported by NIH/NIAID 3R01AI141003-03S1 and NIH/NIAID R01AI158013. C.A.T. is a Pew biomedical scholar and a Kathryn W. Davis Aging Brain scholar and is supported by the NIH Director's New Innovator Award (DP2-AG-067492), the Agilent Early Career Professor Award, and grants from the Edward Mallinckrodt, Jr. Foundation, the IDSA Foundation, the Thyssen Foundation, Polybio Research Foundation, the Kenneth Rainin Foundation, the PennCHOP Microbiome Program, Penn Institute for Immunology, Penn Center for Molecular Studies in Digestive and Liver Diseases (P30-DK-050306), Penn Skin Biology and Diseases Resource-based Center (P30-AR-069589), Penn Diabetes Research Center (P30-DK-019525), Penn Institute on Aging, the Penn Institute for Infectious & Zoonotic Diseases, the University Research Foundation, the Dean's Innovation Fund of the University of Pennsylvania, and a Borrelli Family Lynch Syndrome grant. M. Levy is supported by the NIH Director's New Innovator Award (DP2-AG-067511), an American Cancer Society Scholar Award, The Pew Scholar Award, the Searle Scholars Program, the Edward Mallinckrodt, Jr. Foundation, the W. W. Smith Charitable Trust, the Prevent Cancer Foundation, Polybio Research Foundation, V Foundation, The Burroughs

Wellcome Fund, and grants from the Abramson Cancer Center (P30-CA-016420), the PennCHOP microbiome program, Penn Center for Nutritional Science and Medicine, Penn Coronavirus Center, Penn Institute for Immunology, Penn Center for Molecular Studies in Digestive and Liver Diseases (P30-DK-050306), Penn Center for Precision Medicine, Penn Institute on Aging, Penn Center of Excellence in Environmental Toxicology (P30-ES-013508), and the Borrelli Family Pilot Grant in Lynch Syndrome.

AUTHOR CONTRIBUTIONS

A.C.W. conceived the study, designed and performed the experiments, interpreted the results, and wrote the manuscript. A.S.D., I.C.U., T.O.X., L.D., J.P., Z.E., L.T.I., Jihee Kim, S.L.P., S.W., A.D.M., R.D.P., Junwon Kim, N.B., S.P., K.T., S.M., J.-C.B., S.F.N., M.F.M., B.M.M., M.J.L., B.M., O.D.-M., C.P.C., and H.R. performed experiments. L.L., P.L., and H.C.D. performed computational and statistical analyses. M.T., A.S.H., G.B.-Z., L.B.G., A.E.B., A.R.G., C.K., K.M., L.A.L., M.F., U.O., M.A.-M., A.L.L., A.K., T.J.H., S.G.D., M.J.P., and N.J.M. acquired clinical samples and data. J.H.-M., B.S., K.A.J., K.E.W., and E.J.W. provided essential tools and insights. B.A.A., S.C., C.A.T., and M.L. conceived the study, designed the experiments, interpreted the results, and wrote the manuscript.

DECLARATION OF INTERESTS

E.J.W. is an advisor for Danger Bio, Janssen, New Limit, Marengo, Pluto Immunotherapeutics Related Sciences, Rubius Therapeutics, Santa Ana Bio, Synthekine, and Surface Oncology. E.J.W. is a founder of and holds stock in Surface Oncology, Danger Bio, and Arsenal Biosciences. N.J.M. reports consulting fees from Endpoint Health Inc and AstraZeneca and receives funding from Quantum Leap Healthcare Collaborative outside of the published work.

INCLUSION AND DIVERSITY

We support inclusive, diverse, and equitable conduct of research. One or more of the authors of this paper self-identifies as an underrepresented ethnic minority in their field of research or within their geographical location. One or more of the authors of this paper self-identifies as a member of the LGBTQIA+ community.

Received: August 4, 2022

Revised: July 27, 2023

Accepted: September 13, 2023

Published: October 16, 2023

REFERENCES

1. Choutka, J., Jansari, V., Hornig, M., and Iwasaki, A. (2022). Unexplained post-acute infection syndromes. *Nat. Med.* 28, 911–923. <https://doi.org/10.1038/s41591-022-01810-6>.
2. Al-Aly, Z., Xie, Y., and Bowe, B. (2021). High-dimensional characterization of post-acute sequelae of COVID-19. *Nature* 594, 259–264. <https://doi.org/10.1038/s41586-021-03553-9>.
3. Davis, H.E., McCorkell, L., Vogel, J.M., and Topol, E.J. (2023). Long COVID: major findings, mechanisms and recommendations. *Nat. Rev. Microbiol.* 21, 133–146. <https://doi.org/10.1038/s41579-022-00846-2>.
4. Merad, M., Blish, C.A., Sallusto, F., and Iwasaki, A. (2022). The immunology and immunopathology of COVID-19. *Science* 375, 1122–1127. <https://doi.org/10.1126/science.abm8108>.
5. Pretorius, E., Vlok, M., Venter, C., Bezuidenhout, J.A., Laubscher, G.J., Steenkamp, J., and Kell, D.B. (2021). Persistent clotting protein pathology in Long COVID/Post-Acute Sequelae of COVID-19 (PASC) is accompanied by increased levels of antiplasmin. *Cardiovasc. Diabetol.* 20, 172. <https://doi.org/10.1186/s12933-021-01359-7>.
6. Dani, M., Dirksen, A., Taraborrelli, P., Torocastro, M., Panagopoulos, D., Sutton, R., and Lim, P.B. (2021). Autonomic dysfunction in 'long COVID': rationale, physiology and management strategies. *Clin. Med.* 21, e63–e67. <https://doi.org/10.7861/clinmed.2020-0896>.
7. Shen, B., Yi, X., Sun, Y., Bi, X., Du, J., Zhang, C., Quan, S., Zhang, F., Sun, R., Qian, L., et al. (2020). Proteomic and Metabolomic Characterization of COVID-19 Patient Sera. *Cell* 182, 59–72.e15. <https://doi.org/10.1016/j.cell.2020.05.032>.
8. Shi, D., Yan, R., Lv, L., Jiang, H., Lu, Y., Sheng, J., Xie, J., Wu, W., Xia, J., Xu, K., et al. (2021). The serum metabolome of COVID-19 patients is distinctive and predictive. *Metabolism* 118, 154739. <https://doi.org/10.1016/j.metabol.2021.154739>.
9. Song, J.W., Lam, S.M., Fan, X., Cao, W.J., Wang, S.Y., Tian, H., Chua, G.H., Zhang, C., Meng, F.P., Xu, Z., et al. (2020). Omics-Driven Systems Interrogation of Metabolic Dysregulation in COVID-19 Pathogenesis. *Cell Metab.* 32, 188–202.e5. <https://doi.org/10.1016/j.cmet.2020.06.016>.
10. Thomas, T., Stefanoni, D., Reisz, J.A., Nemkov, T., Bertolone, L., Francis, R.O., Hudson, K.E., Zimring, J.C., Hansen, K.C., Hod, E.A., et al. (2020). COVID-19 infection alters kynurenine and fatty acid metabolism, correlating with IL-6 levels and renal status. *JCI Insight* 5, e140327. <https://doi.org/10.1172/jci.insight.140327>.
11. Xiao, N., Nie, M., Pang, H., Wang, B., Hu, J., Meng, X., Li, K., Ran, X., Long, Q., Deng, H., et al. (2021). Integrated cytokine and metabolite analysis reveals immunometabolic reprogramming in COVID-19 patients with therapeutic implications. *Nat. Commun.* 12, 1618. <https://doi.org/10.1038/s41467-021-21907-9>.
12. Sadlier, C., Albrich, W.C., Neogi, U., Lunjani, N., Horgan, M., O'Toole, P.W., and O'Mahony, L. (2022). Metabolic rewiring and serotonin depletion in patients with postacute sequelae of COVID-19. *Allergy* 77, 1623–1625. <https://doi.org/10.1111/all.15253>.
13. Su, Y., Yuan, D., Chen, D.G., Ng, R.H., Wang, K., Choi, J., Li, S., Hong, S., Zhang, R., Xie, J., et al. (2022). Multiple early factors anticipate post-acute COVID-19 sequelae. *Cell* 185, 881–895.e20. <https://doi.org/10.1016/j.cell.2022.01.014>.
14. Peluso, M.J., Kelly, J.D., Lu, S., Goldberg, S.A., Davidson, M.C., Mathur, S., Durstenfeld, M.S., Spinelli, M.A., Hoh, R., Tai, V., et al. (2022). Persistence, Magnitude, and Patterns of Postacute Symptoms and Quality of Life Following Onset of SARS-CoV-2 Infection: Cohort Description and Approaches for Measurement. *Open Forum Infect. Dis.* 9, ofab640. <https://doi.org/10.1093/ofid/ofab640>.
15. Berger, M., Gray, J.A., and Roth, B.L. (2009). The expanded biology of serotonin. *Annu. Rev. Med.* 60, 355–366. <https://doi.org/10.1146/annurev.med.60.042307.110802>.
16. Yasui, F., Matsumoto, Y., Yamamoto, N., Sanada, T., Honda, T., Munkata, T., Itoh, Y., and Kohara, M. (2022). Infection with the SARS-CoV-2 B.1.351 variant is lethal in aged BALB/c mice. *Sci. Rep.* 12, 4150. <https://doi.org/10.1038/s41598-022-08104-4>.
17. Natarajan, A., Zlitni, S., Brooks, E.F., Vance, S.E., Dahlen, A., Hedlin, H., Park, R.M., Han, A., Schmidtke, D.T., Verma, R., et al. (2022). Gastrointestinal symptoms and fecal shedding of SARS-CoV-2 RNA suggest prolonged gastrointestinal infection. *Med (N Y)* 3, 371–387.e9. <https://doi.org/10.1016/j.medj.2022.04.001>.
18. Swank, Z., Senussi, Y., Manickas-Hill, Z., Yu, X.G., Li, J.Z., Alter, G., and Walt, D.R. (2022). Persistent circulating SARS-CoV-2 spike is associated with post-acute COVID-19 sequelae. *Clin. Infect. Dis.* <https://doi.org/10.1093/cid/ciac722>.
19. Zollner, A., Koch, R., Jukic, A., Pfister, A., Meyer, M., Rössler, A., Kimpel, J., Adolph, T.E., and Tilg, H. (2022). Postacute COVID-19 is Characterized by Gut Viral Antigen Persistence in Inflammatory Bowel Diseases. *Gastroenterology* 163, 495–506.e8. <https://doi.org/10.1053/j.gastro.2022.04.037>.
20. Peluso, M.J., Ryder, D., Flavell, R., Wang, Y., Levi, J., LaFranchi, B.H., Deveau, T.M., Buck, A.M., Munter, S.E., Asare, K.A., et al. (2023). Multimodal Molecular Imaging Reveals Tissue-Based T Cell Activation and Viral RNA Persistence for Up to 2 Years Following COVID-19. Preprint at medRxiv. <https://doi.org/10.1101/2023.07.27.23293177>.

21. Goh, D., Lim, J.C.T., Fernáandez, S.B., Joseph, C.R., Edwards, S.G., Neo, Z.W., Lee, J.N., Caballero, S.G., Lau, M.C., and Yeong, J.P.S. (2022). Case report: Persistence of residual antigen and RNA of the SARS-CoV-2 virus in tissues of two patients with long COVID. *Front. Immunol.* **13**, 939989. <https://doi.org/10.3389/fimmu.2022.939989>.
22. Phetsouphanh, C., Darley, D.R., Wilson, D.B., Howe, A., Munier, C.M.L., Patel, S.K., Juno, J.A., Burrell, L.M., Kent, S.J., Dore, G.J., et al. (2022). Immunological dysfunction persists for 8 months following initial mild-to-moderate SARS-CoV-2 infection. *Nat. Immunol.* **23**, 210–216. <https://doi.org/10.1038/s41590-021-01113-x>.
23. Roager, H.M., and Licht, T.R. (2018). Microbial tryptophan catabolites in health and disease. *Nat. Commun.* **9**, 3294. <https://doi.org/10.1038/s41467-018-05470-4>.
24. Danlos, F.X., Grajeda-Iglesias, C., Durand, S., Sauvat, A., Roumier, M., Cantin, D., Colomba, E., Rohmer, J., Pommeret, F., Baciarello, G., et al. (2021). Metabolomic analyses of COVID-19 patients unravel stage-dependent and prognostic biomarkers. *Cell Death Dis.* **12**, 258. <https://doi.org/10.1038/s41419-021-03540-y>.
25. Valdés, A., Moreno, L.O., Rello, S.R., Orduña, A., Bernardo, D., and Cifuentes, A. (2022). Metabolomics study of COVID-19 patients in four different clinical stages. *Sci. Rep.* **12**, 1650. <https://doi.org/10.1038/s41598-022-05667-0>.
26. Giron, L.B., Dweep, H., Yin, X., Wang, H., Damra, M., Goldman, A.R., Gorman, N., Palmer, C.S., Tang, H.Y., Shaikh, M.W., et al. (2021). Plasma Markers of Disrupted Gut Permeability in Severe COVID-19 Patients. *Front. Immunol.* **12**, 686240. <https://doi.org/10.3389/fimmu.2021.686240>.
27. Giron, L.B., Peluso, M.J., Ding, J., Kenny, G., Zilberstein, N.F., Koshy, J., Hong, K.Y., Rasmussen, H., Miller, G.E., Bishehsari, F., et al. (2022). Markers of fungal translocation are elevated during post-acute sequelae of SARS-CoV-2 and induce NF- κ B signaling. *JCI Insight* **7**, e160989. <https://doi.org/10.1172/jci.insight.160989>.
28. Fortier, M.E., Kent, S., Ashdown, H., Poole, S., Boksa, P., and Luheshi, G.N. (2004). The viral mimic, polyinosinic:polycytidylic acid, induces fever in rats via an interleukin-1-dependent mechanism. *Am. J. Physiol. Regul. Integr. Comp. Physiol.* **287**, R759–R766. <https://doi.org/10.1152/ajpregu.00293.2004>.
29. Zhu, X., Levasseur, P.R., Michaelis, K.A., Burfeind, K.G., and Marks, D.L. (2016). A distinct brain pathway links viral RNA exposure to sickness behavior. *Sci. Rep.* **6**, 29885. <https://doi.org/10.1038/srep29885>.
30. Lamers, M.M., Beumer, J., van der Vaart, J., Knoops, K., Puschhof, J., Breugem, T.I., Ravelli, R.B.G., Paul van Schayck, J., Mykityn, A.Z., Duimel, H.Q., et al. (2020). SARS-CoV-2 productively infects human gut enterocytes. *Science* **369**, 50–54. <https://doi.org/10.1126/science.abc1669>.
31. Gaebler, C., Wang, Z., Lorenzi, J.C.C., Muecksch, F., Finkin, S., Tokuyama, M., Cho, A., Jankovic, M., Schaefer-Babajew, D., Oliveira, T.Y., et al. (2021). Evolution of antibody immunity to SARS-CoV-2. *Nature* **591**, 639–644. <https://doi.org/10.1038/s41586-021-03207-w>.
32. Singer, D., Camargo, S.M.R., Ramadan, T., Schäfer, M., Mariotta, L., Herzog, B., Huggel, K., Wolfer, D., Werner, S., Penninger, J.M., and Verrey, F. (2012). Defective intestinal amino acid absorption in Ace2 null mice. *Am. J. Physiol. Gastrointest. Liver Physiol.* **303**, G686–G695. <https://doi.org/10.1152/ajpgi.00140.2012>.
33. Hashimoto, T., Perlot, T., Rehman, A., Trichereau, J., Ishiguro, H., Paolino, M., Sigl, V., Hanada, T., Hanada, R., Lipinski, S., et al. (2012). ACE2 links amino acid malnutrition to microbial ecology and intestinal inflammation. *Nature* **487**, 477–481. <https://doi.org/10.1038/nature11228>.
34. Wolf, K., Braun, A., Haining, E.J., Tseng, Y.L., Kraft, P., Schuhmann, M.K., Gotru, S.K., Chen, W., Hermanns, H.M., Stoll, G., et al. (2016). Partially Defective Store Operated Calcium Entry and Hem(ITAM) Signaling in Platelets of Serotonin Transporter Deficient Mice. *PLoS One* **11**, e0147664. <https://doi.org/10.1371/journal.pone.0147664>.
35. Rivadeneyra, L., Pozner, R.G., Meiss, R., Fondevila, C., Gómez, R.M., and Schattner, M. (2015). Poly (I:C) downregulates platelet production and function through type I interferon. *Thromb. Haemost.* **114**, 982–993. <https://doi.org/10.1160/TH14-11-0951>.
36. Lee, E., Kim, M., Jeon, K., Lee, J., Lee, J.S., Kim, H.S., Kang, H.J., and Lee, Y.K. (2019). Mean Platelet Volume, Platelet Distribution Width, and Platelet Count, in Connection with Immune Thrombocytopenic Purpura and Essential Thrombocytopenia. *Lab. Med.* **50**, 279–285. <https://doi.org/10.1093/labmed/lmy082>.
37. Norrasethada, L., Khumpoo, W., Rattarittamrong, E., Rattanathammethee, T., Chai-Adisaksopha, C., and Tantiworawit, A. (2019). The use of mean platelet volume for distinguishing the causes of thrombocytopenia in adult patients. *Hematol. Rep.* **11**, 7732. <https://doi.org/10.4081/hr.2019.7732>.
38. Schmoeller, D., Picarelli, M.M., Paz Munhoz, T., Poli de Figueiredo, C.E., and Staub, H.L. (2017). Mean Platelet Volume and Immature Platelet Fraction in Autoimmune Disorders. *Front. Med.* **4**, 146. <https://doi.org/10.3389/fmed.2017.00146>.
39. Anabel, A.S., Eduardo, P.C., Pedro Antonio, H.C., Carlos, S.M., Juana, N.M., Honorio, T.A., Nicolás, V.S., and Sergio Roberto, A.R. (2014). Human platelets express Toll-like receptor 3 and respond to poly I:C. *Hum. Immunol.* **75**, 1244–1251. <https://doi.org/10.1016/j.humimm.2014.09.013>.
40. D’Atri, L.P., Etulain, J., Rivadeneyra, L., Lapponi, M.J., Centurion, M., Cheng, K., Yin, H., and Schattner, M. (2015). Expression and functionality of Toll-like receptor 3 in the megakaryocytic lineage. *J. Thromb. Haemost.* **13**, 839–850. <https://doi.org/10.1111/jth.12842>.
41. Morodomi, Y., Kanaji, S., Won, E., Ruggeri, Z.M., and Kanaji, T. (2020). Mechanisms of anti-GPIIb/IIIa antibody-induced thrombocytopenia in mice. *Blood* **135**, 2292–2301. <https://doi.org/10.1182/blood.2019003770>.
42. Kamal, A.H., Tefferi, A., and Pruthi, R.K. (2007). How to interpret and pursue an abnormal prothrombin time, activated partial thromboplastin time, and bleeding time in adults. *Mayo Clin. Proc.* **82**, 864–873. <https://doi.org/10.4065/82.7.864>.
43. Antunes, M., and Biala, G. (2012). The novel object recognition memory: neurobiology, test procedure, and its modifications. *Cogn. Process.* **13**, 93–110. <https://doi.org/10.1007/s10339-011-0430-z>.
44. Costello, D.A., and Lynch, M.A. (2013). Toll-like receptor 3 activation modulates hippocampal network excitability, via glial production of interferon-beta. *Hippocampus* **23**, 696–707. <https://doi.org/10.1002/hipo.22129>.
45. Chen, C., Gao, R., Li, M., Wang, Q., Chen, H., Zhang, S., Mao, X., Behensky, A., Zhang, Z., Gan, L., et al. (2019). Extracellular RNAs-TLR3 signaling contributes to cognitive decline in a mouse model of postoperative cognitive dysfunction. *Brain Behav. Immun.* **80**, 439–451. <https://doi.org/10.1016/j.bbi.2019.04.024>.
46. Clark, R.E., Zola, S.M., and Squire, L.R. (2000). Impaired recognition memory in rats after damage to the hippocampus. *J. Neurosci.* **20**, 8853–8860. <https://doi.org/10.1523/JNEUROSCI.20-23-08853.2000>.
47. Douaud, G., Lee, S., Alfaro-Almagro, F., Arthofer, C., Wang, C., McCarthy, P., Lange, F., Andersson, J.L.R., Griffanti, L., Duff, E., et al. (2022). SARS-CoV-2 is associated with changes in brain structure in UK Biobank. *Nature* **604**, 697–707. <https://doi.org/10.1038/s41586-022-04569-5>.
48. Soung, A.L., Vanderheiden, A., Nordvig, A.S., Sissoko, C.A., Canoll, P., Mariani, M.B., Jiang, X., Bricker, T., Rosoklija, G.B., Arango, V., et al. (2022). COVID-19 induces CNS cytokine expression and loss of hippocampal neurogenesis. *Brain* **145**, 4193–4201. <https://doi.org/10.1093/brain/awac270>.
49. Alenina, N., and Klempin, F. (2015). The role of serotonin in adult hippocampal neurogenesis. *Behav. Brain Res.* **277**, 49–57. <https://doi.org/10.1016/j.bbr.2014.07.038>.

50. Richter-Levin, G., and Segal, M. (1996). Serotonin, aging and cognitive functions of the hippocampus. *Rev. Neurosci.* 7, 103–113. <https://doi.org/10.1515/revneuro.1996.7.2.103>.
51. Winterer, J., Stempel, A.V., Dugladze, T., Földy, C., Maziashvili, N., Zivkovic, A.R., Priller, J., Soltesz, I., Gloveli, T., and Schmitz, D. (2011). Cell-type-specific modulation of feedback inhibition by serotonin in the hippocampus. *J. Neurosci.* 31, 8464–8475. <https://doi.org/10.1523/JNEUROSCI.6382-10.2011>.
52. Kupari, J., Häring, M., Agirre, E., Castelo-Branco, G., and Erfors, P. (2019). An Atlas of Vagal Sensory Neurons and Their Molecular Specialization. *Cell Rep.* 27, 2508–2523.e4. <https://doi.org/10.1016/j.celrep.2019.04.096>.
53. Bowe, B., Xie, Y., and Al-Aly, Z. (2023). Postacute sequelae of COVID-19 at 2 years. *Nat. Med.* 29, 2347–2357. <https://doi.org/10.1038/s41591-023-02521-2>.
54. Azzolini, E., Levi, R., Sarti, R., Pozzi, C., Mollura, M., Mantovani, A., and Rescigno, M. (2022). Association Between BNT162b2 Vaccination and Long COVID After Infections Not Requiring Hospitalization in Health Care Workers. *JAMA* 328, 676–678. <https://doi.org/10.1001/jama.2022.11691>.
55. Xie, Y., Bowe, B., and Al-Aly, Z. (2021). Burdens of post-acute sequelae of COVID-19 by severity of acute infection, demographics and health status. *Nat. Commun.* 12, 6571. <https://doi.org/10.1038/s41467-021-26513-3>.
56. Al-Aly, Z., Bowe, B., and Xie, Y. (2022). Long COVID after breakthrough SARS-CoV-2 infection. *Nat. Med.* 28, 1461–1467. <https://doi.org/10.1038/s41591-022-01840-0>.
57. Palm, W., and Thompson, C.B. (2017). Nutrient acquisition strategies of mammalian cells. *Nature* 546, 234–242. <https://doi.org/10.1038/nature22379>.
58. Platten, M., Nollen, E.A.A., Röhrig, U.F., Fallarino, F., and Opitz, C.A. (2019). Tryptophan metabolism as a common therapeutic target in cancer, neurodegeneration and beyond. *Nat. Rev. Drug Discov.* 18, 379–401. <https://doi.org/10.1038/s41573-019-0016-5>.
59. Ghebrehiwet, B., and Peerschke, E.I. (2020). Complement and coagulation: key triggers of COVID-19-induced multiorgan pathology. *J. Clin. Invest.* 130, 5674–5676. <https://doi.org/10.1172/JCI142780>.
60. Pasini, E., Corsetti, G., Romano, C., Scarabelli, T.M., Chen-Scarabelli, C., Saravolatz, L., and Dioguardi, F.S. (2021). Serum Metabolic Profile in Patients With Long-Covid (PASC) Syndrome: Clinical Implications. *Front. Med.* 8, 714426. <https://doi.org/10.3389/fmed.2021.714426>.
61. Spyropoulos, A.C., and Bonaca, M.P. (2022). Studying the coagulopathy of COVID-19. *Lancet* 399, 118–119. [https://doi.org/10.1016/S0140-6736\(21\)01906-1](https://doi.org/10.1016/S0140-6736(21)01906-1).
62. Proal, A.D., and VanElzakker, M.B. (2021). Long COVID or Post-acute Sequelae of COVID-19 (PASC): An Overview of Biological Factors That May Contribute to Persistent Symptoms. *Front. Microbiol.* 12, 698169. <https://doi.org/10.3389/fmicb.2021.698169>.
63. Aschman, T., Mothes, R., Heppner, F.L., and Radbruch, H. (2022). What SARS-CoV-2 does to our brains. *Immunity* 55, 1159–1172. <https://doi.org/10.1016/j.immuni.2022.06.013>.
64. Frontera, J.A., and Simon, N.M. (2022). Bridging Knowledge Gaps in the Diagnosis and Management of Neuropsychiatric Sequelae of COVID-19. *JAMA Psychiatr.* 79, 811–817. <https://doi.org/10.1001/jamapsychiatry.2022.1616>.
65. Fernandez-Castaneda, A., Lu, P., Geraghty, A.C., Song, E., Lee, M.H., Wood, J., O’Dea, M.R., Dutton, S., Shamardani, K., Nwangwu, K., et al. (2022). Mild respiratory COVID can cause multi-lineage neural cell and myelin dysregulation. *Cell* 185, 2452–2468.e2416. <https://doi.org/10.1016/j.cell.2022.06.008>.
66. Bin, N.R., Prescott, S.L., Horio, N., Wang, Y., Chiu, I.M., and Liberles, S.D. (2023). An airway-to-brain sensory pathway mediates influenza-induced sickness. *Nature* 615, 660–667. <https://doi.org/10.1038/s41586-023-05796-0>.
67. McVey Neufeld, K.A., Bienenstock, J., Bharwani, A., Champagne-Jorgensen, K., Mao, Y., West, C., Liu, Y., Surette, M.G., Kunze, W., and Forsythe, P. (2019). Oral selective serotonin reuptake inhibitors activate vagus nerve dependent gut-brain signalling. *Sci. Rep.* 9, 14290. <https://doi.org/10.1038/s41598-019-50807-8>.
68. VanElzakker, M.B. (2013). Chronic fatigue syndrome from vagus nerve infection: a psychoneuroimmunological hypothesis. *Med. Hypotheses* 81, 414–423. <https://doi.org/10.1016/j.mehy.2013.05.034>.
69. Bonnet, U., and Juckel, G. (2022). COVID-19 Outcomes: Does the Use of Psychotropic Drugs Make a Difference? Accumulating Evidence of a Beneficial Effect of Antidepressants—A Scoping Review. *J. Clin. Psychopharmacol.* 42, 284–292. <https://doi.org/10.1097/JCP.0000000000001543>.
70. Lee, T.C., Vigod, S., Bortolussi-Courval, É., Hanula, R., Boulware, D.R., Lenze, E.J., Reiersen, A.M., and McDonald, E.G. (2022). Fluvoxamine for Outpatient Management of COVID-19 to Prevent Hospitalization: A Systematic Review and Meta-analysis. *JAMA Netw. Open* 5, e226269. <https://doi.org/10.1001/jamanetworkopen.2022.6269>.
71. Mahdi, M., Hermán, L., Réthelyi, J.M., and Bálint, B.L. (2022). Potential Role of the Antidepressants Fluoxetine and Fluvoxamine in the Treatment of COVID-19. *Int. J. Mol. Sci.* 23, 3812. <https://doi.org/10.3390/ijms23073812>.
72. Reis, G., Dos Santos Moreira-Silva, E.A., Silva, D.C.M., Thabane, L., Milagres, A.C., Ferreira, T.S., Dos Santos, C.V.Q., de Souza Campos, V.H., Nogueira, A.M.R., de Almeida, A.P.F.G., et al. (2022). Effect of early treatment with fluvoxamine on risk of emergency care and hospitalisation among patients with COVID-19: the TOGETHER randomised, platform clinical trial. *Lancet. Glob. Health* 10, e42–e51. [https://doi.org/10.1016/S2214-109X\(21\)00448-4](https://doi.org/10.1016/S2214-109X(21)00448-4).
73. Wen, W., Chen, C., Tang, J., Wang, C., Zhou, M., Cheng, Y., Zhou, X., Wu, Q., Zhang, X., Feng, Z., et al. (2022). Efficacy and safety of three new oral antiviral treatment (molnupiravir, fluvoxamine and Paxlovid) for COVID-19: a meta-analysis. *Ann. Med.* 54, 516–523. <https://doi.org/10.1080/07853890.2022.2034936>.
74. Zheng, W., Sun, H.L., Cai, H., Zhang, Q., Ng, C.H., and Xiang, Y.T. (2022). Antidepressants for COVID-19: A systematic review. *J. Affect. Disord.* 307, 108–114. <https://doi.org/10.1016/j.jad.2022.03.059>.
75. Brown, L.A., Ballentine, E., Zhu, Y., McGinley, E.L., Pezzin, L., and Abramoff, B. (2022). The unique contribution of depression to cognitive impairment in Post-Acute Sequelae of SARS-CoV-2 infection. *Brain Behav. Immun. Health* 22, 100460. <https://doi.org/10.1016/j.bbih.2022.100460>.
76. Hoffmann, M., Kleine-Weber, H., Schroeder, S., Krüger, N., Herrler, T., Erichsen, S., Schiergens, T.S., Herrler, G., Wu, N.H., Nitsche, A., et al. (2020). SARS-CoV-2 Cell Entry Depends on ACE2 and TMPRSS2 and Is Blocked by a Clinically Proven Protease Inhibitor. *Cell* 181, 271–280.e8. <https://doi.org/10.1016/j.cell.2020.02.052>.
77. Cui, L., Lee, Y.H., Thein, T.L., Fang, J., Pang, J., Ooi, E.E., Leo, Y.S., Ong, C.N., and Tannenbaum, S.R. (2016). Serum Metabolomics Reveals Serotonin as a Predictor of Severe Dengue in the Early Phase of Dengue Fever. *PLoS Negl. Trop. Dis.* 10, e0004607. <https://doi.org/10.1371/journal.pntd.0004607>.
78. Seet, R.C.S., Quek, A.M.L., and Lim, E.C.H. (2007). Post-infectious fatigue syndrome in dengue infection. *J. Clin. Virol.* 38, 1–6. <https://doi.org/10.1016/j.jcv.2006.10.011>.
79. Lood, C., Tydén, H., Gullstrand, B., Klint, C., Wengglén, C., Nielsen, C.T., Heegaard, N.H.H., Jönsen, A., Kahn, R., and Bengtsson, A.A. (2015). Type I interferon-mediated skewing of the serotonin synthesis is associated with severe disease in systemic lupus erythematosus. *PLoS One* 10, e0125109. <https://doi.org/10.1371/journal.pone.0125109>.
80. San Hernandez, A.M., Singh, C., Valero, D.J., Nisar, J., Trujillo Ramirez, J.I., Kothari, K.K., Isola, S., and Gordon, D.K. (2020). Multiple Sclerosis

- and Serotonin: Potential Therapeutic Applications. *Cureus* 12, e11293. <https://doi.org/10.7759/cureus.11293>.
81. Meyerhoff, J., and Dorsch, C.A. (1981). Decreased platelet serotonin levels in systemic lupus erythematosus. *Arthritis Rheum.* 24, 1495–1500. <https://doi.org/10.1002/art.1780241207>.
82. Thompson, R.C., Simons, N.W., Wilkins, L., Cheng, E., Del Valle, D.M., Hoffman, G.E., Cervia, C., Fennessy, B., Mouskas, K., Francoeur, N.J., et al. (2023). Molecular states during acute COVID-19 reveal distinct etiologies of long-term sequelae. *Nat. Med.* 29, 236–246. <https://doi.org/10.1038/s41591-022-02107-4>.
83. Mathew, D., Giles, J.R., Baxter, A.E., Oldridge, D.A., Greenplate, A.R., Wu, J.E., Alanio, C., Kuri-Cervantes, L., Pampena, M.B., D'Andrea, K., et al. (2020). Deep immune profiling of COVID-19 patients reveals distinct immunotypes with therapeutic implications. *Science* 369, eabc8511. <https://doi.org/10.1126/science.abc8511>.
84. Reilly, J.P., Anderson, B.J., Hudock, K.M., Dunn, T.G., Kazi, A., Tommasini, A., Charles, D., Shashaty, M.G.S., Mikkelsen, M.E., Christie, J.D., and Meyer, N.J. (2016). Neutropenic sepsis is associated with distinct clinical and biological characteristics: a cohort study of severe sepsis. *Crit. Care* 20, 222. <https://doi.org/10.1186/s13054-016-1398-y>.
85. Klover, P.J., Muller, W.J., Robinson, G.W., Pfeiffer, R.M., Yamaji, D., and Hennighausen, L. (2010). Loss of STAT1 from mouse mammary epithelium results in an increased Neu-induced tumor burden. *Neoplasia* 12, 899–905. <https://doi.org/10.1593/neo.10716>.
86. Peluso, M.J., Deitchman, A.N., Torres, L., Iyer, N.S., Munter, S.E., Nixon, C.C., Donatelli, J., Thanh, C., Takahashi, S., Hakim, J., et al. (2021). Long-term SARS-CoV-2-specific immune and inflammatory responses in individuals recovering from COVID-19 with and without post-acute symptoms. *Cell Rep.* 36, 109518. <https://doi.org/10.1016/j.celrep.2021.109518>.
87. Miyoshi, H., and Stappenbeck, T.S. (2013). In vitro expansion and genetic modification of gastrointestinal stem cells in spheroid culture. *Nat. Protoc.* 8, 2471–2482. <https://doi.org/10.1038/nprot.2013.153>.
88. Sato, T., Stange, D.E., Ferrante, M., Vries, R.G.J., Van Es, J.H., Van den Brink, S., Van Houdt, W.J., Pronk, A., Van Gorp, J., Siersema, P.D., and Clevers, H. (2011). Long-term expansion of epithelial organoids from human colon, adenoma, adenocarcinoma, and Barrett's epithelium. *Gastroenterology* 141, 1762–1772. <https://doi.org/10.1053/j.gastro.2011.07.050>.
89. Mizutani, T., and Clevers, H. (2020). Primary Intestinal Epithelial Organoid Culture. *Methods Mol. Biol.* 2171, 185–200. https://doi.org/10.1007/978-1-0716-0747-3_11.
90. De Cuyper, I.M., Meinders, M., van de Vijver, E., de Korte, D., Porcelijn, L., de Haas, M., Eble, J.A., Seeger, K., Rutella, S., Pagliara, D., et al. (2013). A novel flow cytometry-based platelet aggregation assay. *Blood* 121, e70–e80. <https://doi.org/10.1182/blood-2012-06-437723>.
91. Han, W., and de Araujo, I.E. (2021). Dissection and surgical approaches to the mouse jugular-nodose ganglia. *STAR Protoc.* 2, 100474. <https://doi.org/10.1016/j.xpro.2021.100474>.
92. Lin, Y.T., and Chen, J.C. (2018). Dorsal Root Ganglia Isolation and Primary Culture to Study Neurotransmitter Release. *J. Vis. Exp.* <https://doi.org/10.3791/57569>.
93. Lanfear, D.E., Gibbs, J.J., Li, J., She, R., Petucci, C., Culver, J.A., Tang, W.H.W., Pinto, Y.M., Williams, L.K., Sabbah, H.N., and Gardell, S.J. (2017). Targeted Metabolomic Profiling of Plasma and Survival in Heart Failure Patients. *JACC. Heart Fail.* 5, 823–832. <https://doi.org/10.1016/j.jchf.2017.07.009>.
94. Gardell, S.J., Zhang, X., Kapoor, N., Petucci, C., and Coen, P.M. (2019). Metabolomics Analyses of Muscle Atrophy Induced by Hind Limb Unloading. *Methods Mol. Biol.* 1996, 297–309. https://doi.org/10.1007/978-1-4939-9488-5_22.
95. Odorizzi, P.M., Pauken, K.E., Paley, M.A., Sharpe, A., and Wherry, E.J. (2015). Genetic absence of PD-1 promotes accumulation of terminally differentiated exhausted CD8+ T cells. *J. Exp. Med.* 212, 1125–1137. <https://doi.org/10.1084/jem.20142237>.
96. Burzynski, L.C., Pugh, N., and Clarke, M.C.H. (2019). Platelet Isolation and Activation Assays. *Bio. Protoc.* 9, e3405. <https://doi.org/10.21769/BioProtoc.3405>.
97. Mootha, V.K., Lindgren, C.M., Eriksson, K.F., Subramanian, A., Sihag, S., Lehar, J., Puigserver, P., Carlsson, E., Ridderstråle, M., Laurila, E., et al. (2003). PGC-1alpha-responsive genes involved in oxidative phosphorylation are coordinately downregulated in human diabetes. *Nat. Genet.* 34, 267–273. <https://doi.org/10.1038/ng1180>.
98. Subramanian, A., Tamayo, P., Mootha, V.K., Mukherjee, S., Ebert, B.L., Gillette, M.A., Paulovich, A., Pomeroy, S.L., Golub, T.R., Lander, E.S., and Mesirov, J.P. (2005). Gene set enrichment analysis: a knowledge-based approach for interpreting genome-wide expression profiles. *Proc. Natl. Acad. Sci. USA* 102, 15545–15550. <https://doi.org/10.1073/pnas.0506580102>.
99. Stuart, T., Butler, A., Hoffman, P., Hafemeister, C., Papalexi, E., Mauck, W.M., 3rd, Hao, Y., Stoeckius, M., Smibert, P., and Satija, R. (2019). Comprehensive Integration of Single-Cell Data. *Cell* 177, 1888–1902.e21. <https://doi.org/10.1016/j.cell.2019.05.031>.
100. Hafemeister, C., and Satija, R. (2019). Normalization and variance stabilization of single-cell RNA-seq data using regularized negative binomial regression. *Genome Biol.* 20, 296. <https://doi.org/10.1186/s13059-019-1874-1>.

STAR★METHODS

KEY RESOURCES TABLE

REAGENT or RESOURCE	SOURCE	IDENTIFIER
Antibodies		
Anti-doublecortin antibody	Abcam	ab18723; RRID:AB_732011
Anti-NeuN Antibody, clone A60	Millipore Sigma	MAB377; RRID:AB_2298772
Anti-mouse GPIIb α	Emfret	R300; RRID:AB_2721041
Anti-mouse IFNAR-1 antibody	Bio X Cell	BE0241; RRID:AB_2687723
APC anti-mouse CD9 Antibody	Biolegend	124811; RRID:AB_2783070
APC Rat Anti-Mouse CD41	Biolegend	133913; RRID:AB_11126751
c-Fos (9F6) Rabbit mAb	Cell Signaling Technology	2250; RRID:AB_2247211
Donkey anti-Mouse IgG (H + L) Highly Cross-Adsorbed Secondary Antibody, Alexa Fluor™ 488	Thermo Fisher Scientific	A-21202; RRID:AB_141607
Donkey anti-Rabbit IgG (H + L) Highly Cross-Adsorbed Secondary Antibody, Alexa Fluor™ 647	Thermo Fisher Scientific	A-31573; RRID:AB_2536183
FITC Rat Anti-Mouse CD62P	BD	561923; RRID:AB_10896149
GAPDH (D16H11) XP® Rabbit mAb	Cell Signaling Technology	5174S; RRID:AB_10622025
Goat anti-Human IgM-HRP	SouthernBiotech	2020-05; RRID:AB_2795603
Goat anti-Rabbit IgG (H + L) Cross-Adsorbed Secondary Antibody, Alexa Fluor™ 488	Invitrogen	A-11008; RRID:AB_143165
Ki-67 Monoclonal Antibody (SolA15)	eBioscience	14-5698-82; RRID:AB_10854564
Non-immune rat immunoglobulins (IgG)	Emfret	C301; RRID:AB_2734715
PE anti-mouse CD9 Antibody	Biolegend	124805; RRID:AB_1279327
Peroxidase AffiniPure Goat Anti-Human IgG (H + L)	Jackson ImmunoResearch Laboratories	109-035-088; RRID:AB_2337584
Phospho-Stat1 (Tyr701) (58D6) Rabbit mAb	Cell Signaling Technology	9167S; RRID:AB_561284
Rabbit anti-chromogranin A antibody	Novus Biologicals	NB120-15160
Stat1 (D1K9Y) Rabbit mAb	Cell Signaling Technology	14994S; RRID:AB_2737027
β -Actin Antibody (C4)	Santa Cruz Biotechnology	sc-47778; RRID:AB_2714189
Bacterial and virus strains		
pAAV-hSyn-DIO-hM3Dq-mCherry	Addgene	44361
LCMV (Armstrong strain)	John Wherry, University of Pennsylvania	N/A
LCMV (Clone 13 strain)	John Wherry, University of Pennsylvania	N/A
SARS-CoV-2, Isolate B.1.351	Andy Pekosz, Johns Hopkins University	N/A
SARS-CoV-2, Isolate USA-WA1/2020	BEI Resources	NR-52281
Vesicular stomatitis virus (Indiana strain)	Sara Cherry, University of Pennsylvania	N/A
Biological samples		
Acute and recovered COVID-19 cohort plasma samples	Mathew et al. ⁸³	N/A
Healthy and PASC stool samples	This study	N/A
Healthy cohort plasma samples	Una O'Doherty, University of Pennsylvania	N/A
Human autopsy tissues	This study	N/A
RUSH PASC cohort plasma samples	Giron et al. ²⁷	N/A
UCSF LIINC cohort plasma samples	Peluso et al. ¹⁴	N/A
UNCOVER cohort plasma samples	Su et al. ¹³	N/A
UPenn PASC cohort plasma samples	This study	N/A

(Continued on next page)

Continued

REAGENT or RESOURCE	SOURCE	IDENTIFIER
Viremia cohort plasma samples	Reilly et al. ⁸⁴	N/A
Chemicals, peptides, and recombinant proteins		
L-tryptophan (13C11, 99%)	Cambridge Isotope Laboratories	CLM-4290-H-0.1
1-(3-Chlorophenyl)biguanide hydrochloride	Tocris	440
4-Chloro-DL-phenylalanine methyl ester hydrochloride	Sigma-Aldrich	C3635
5-HT	Millipore Sigma	14927
5-hydroxy-L-tryptophan	Cayman Chemical Company	20539
680C91	Selleck Chemicals	S8997
Capsaicin	Sigma-Aldrich	M2028
Clozapine N-oxide hydrochloride	Sigma-Aldrich	SML2304
Collagenase 1A	Gibco	17100017
Dithiothreitol (DTT)	Sigma-Aldrich	1.02E+10
Fluoxetine oral solution, USP	Aurobindo	NDC 65862-306-12
Fura-2-AM	Thermo Fisher Scientific	F-1221
Gly-Pro-Arg-Pro	Sigma-Aldrich	G1895
Glycyl-L-tryptophan hydrate	VWR	100276-390
HEPES	Thermo Fisher Scientific	5-630-080
HMW poly(I:C)	InvivoGen	tlrl-pic
IKK-16	Selleck Chemicals	No.S2882
L-tryptophan	Sigma-Aldrich	T8941
LMW poly(I:C)	InvivoGen	tlrl-picw
Mouse NGF 7S Subunit protein	Gibco	549 13-290-010
N-tert-Butyldimethylsilyl-N-methyltrifluoroacetamide	Sigma-Aldrich	394882
Nickel-nitrilotriacetic acid (Ni-NTA) resin	Qiagen	30210
Penicillin/streptomycin	Thermo Fisher Scientific	15140122
Phenelzine sulfate salt	Sigma-Aldrich	P6777
Poly-L-lysine	Sigma Aldrich	P4707
Poly(I:C)	Sigma-Aldrich	P1530
Recombinant Mouse IFN- α	BioLegend	752802
Recombinant Mouse IFN- β 1	BioLegend	581302
Sodium pyruvate	Corning	MT25000CI
SureBlue 3,3',5,5'-tetramethylbenzidine substrate	KPL	5120-0075
Thrombin	Sigma-Aldrich	T4648
Critical commercial assays		
5-HIAA ELISA kits	Abnova	KA1881
Fibrinogen ELISA kits	Abcam	ab213478
High-Capacity cDNA Reverse Transcription kits	Thermo Fisher Scientific	43-688-13
Kynurenine ELISA kits	Abnova	KA6140
LUNA Universal PCR kit	New England Biolabs	M3003E
Pierce BCA Protein Assay Kit	Thermo Fisher Scientific	23225
QuantiFast SYBR Green PCR kit	Qiagen	204056
RNAeasy mini kits	Qiagen	74104
Serotonin ELISA kits	Novus biologicals	KA1894
Thrombin-Antithrombin Complexes ELISA kits	Abcam	ab137994
Tissue factor ELISA kits	Abcam	ab214091

(Continued on next page)

Continued

REAGENT or RESOURCE	SOURCE	IDENTIFIER
Tryptophan ELISA kits	Novus biologicals	KA11916
Waters AccQTag Ultra derivatization kit	Waters corporation	86003836
Viral RNA Mini Kit	Qiagen	52906
Deposited data		
Human intestinal organoid RNA-sequencing	Lamers et al. ³⁰	GSE149312
Metabolomics of COVID-19 patients	Shen et al., Shi et al., Song et al., Thomas et al., and Xiao et al. ^{7–11}	N/A
Metabolomics of patients with PASC	Sadlier et al. ¹²	N/A
Single-cell RNA-seq of vagal neurons	Kupari et al. ⁵²	GSE124312
RNA-seq of ileum from poly(I:C)-treated mice	This study	PRJNA1007416
Experimental models: Organisms/strains		
C57BL/6J	The Jackson Laboratory	000664
TLR3 ^{-/-}	The Jackson Laboratory	005217
ACE2 ^{-/-}	Taconic Biosciences	18180
IDO1 ^{-/-}	The Jackson Laboratory	005867
IFNAR1 ^{-/-}	The Jackson Laboratory	028288
K18-HuACE2	The Jackson Laboratory	034860
Phox2b-Cre	The Jackson Laboratory	016223
STAT1 ^{-/-}	The Jackson Laboratory	012606
STAT1 ^{flox/flox}	Klover et al., Neoplasia, 2010 ⁸⁵	Klover et al. ⁸⁵
Villin-cre ^{ERT2}	The Jackson Laboratory	020282
Oligonucleotides		
Forward primer for 18S qPCR: 5'-AACCCGTTGAACCCATT-3'	Integrated DNA technologies	N/A
Reverse primer for 18S qPCR: 5'-CCATCCAATCGGTAGTAGCG-3'	Integrated DNA technologies	N/A
Forward primer for Ddc qPCR: 5'-TAGCTGACTATCTGGATGGCAT-3'	Integrated DNA technologies	N/A
Reverse primer for Ddc qPCR: 5'-GTCCTCGTATGTTTCTGGCTC-3'	Integrated DNA technologies	N/A
Forward primer for <i>lfit1</i> qPCR: 5'-CAGAAGCACACATTGAAGAA-3'	Integrated DNA technologies	N/A
Reverse primer for <i>lfit1</i> qPCR: 5'-TGTAAGTAGCCAGAGGAAGG-3'	Integrated DNA technologies	N/A
Forward primer for <i>lfit2</i> qPCR: 5'-GGGAAAGCAGAGGAAATCAA-3'	Integrated DNA technologies	N/A
Reverse primer for <i>lfit2</i> qPCR: 5'-TGAAAGTTGCCATACAGAAG-3'	Integrated DNA technologies	N/A
Forward primer for <i>lfit3</i> qPCR: 5'-GCCGTTACAGGAAATACTGG-3'	Integrated DNA technologies	N/A
Reverse primer for <i>lfit3</i> qPCR: 5'-CCTCAACATCGGGGCTCT-3'	Integrated DNA technologies	N/A
Forward primer for <i>Mx1</i> qPCR: 5'-GACTACCACTGAGATGACCCAGC-3'	Integrated DNA technologies	N/A
Reverse primer for <i>Mx1</i> qPCR: 5'-ATTCCTCCCCAAATGTTTCA-3'	Integrated DNA technologies	N/A
Forward primer for <i>Nsp14</i> qPCR: 5'-TGGGGYTTACRGGTAACCT-3'	Integrated DNA technologies	N/A
Reverse primer for <i>Nsp14</i> qPCR: 5'-AACRCGCTTAACAAAGCACTC-3'	Integrated DNA technologies	N/A

(Continued on next page)

Continued

REAGENT or RESOURCE	SOURCE	IDENTIFIER
Forward primer for <i>Oas1b</i> qPCR: 5'-TTCTACGCCAATCTCATCAGTG-3'	Integrated DNA technologies	N/A
Reverse primer for <i>Oas1b</i> qPCR: 5'-GGTCCCCAGCTTCTCCTTAC-3'	Integrated DNA technologies	N/A
Forward primer for <i>Rpl32</i> qPCR: 5'-TTCCTGGTCCACAATGTCAA-3'	Integrated DNA technologies	N/A
Reverse primer for <i>Rpl32</i> qPCR: 5'-GGCTTTTCGGTTCTTAGAGGA-3'	Integrated DNA technologies	N/A
Forward primer for <i>Slc18a1</i> qPCR: 5'-GTCCCGAAGCTGGTGTG-3'	Integrated DNA technologies	N/A
Reverse primer for <i>Slc18a1</i> qPCR: 5'-ACAGTGAGCAGCATATTGTCC-3'	Integrated DNA technologies	N/A
Forward primer for <i>Slc3a2</i> qPCR: 5'-ACGGTGTGGATGGTTTCCAAT-3'	Integrated DNA technologies	N/A
Reverse primer for <i>Slc3a2</i> qPCR: 5'-TCCCTGCAATCAAAAGCCTGT-3'	Integrated DNA technologies	N/A
Forward primer for <i>Slc6a14</i> qPCR: 5'-GACAGTTCATCCGAGAACTTC-3'	Integrated DNA technologies	N/A
Reverse primer for <i>Slc6a14</i> qPCR: 5'-ATTGCCCAATCCCACTGCAT-3'	Integrated DNA technologies	N/A
Forward primer for <i>Slc6a19</i> qPCR: 5'-AACGCTCATGTATAGCATCTGG-3'	Integrated DNA technologies	N/A
Reverse primer for <i>Slc6a19</i> qPCR: 5'-CAGCCACAGTGACCACAAC-3'	Integrated DNA technologies	N/A
Forward primer for <i>Slc6a4</i> qPCR: 5'-GACAGGGGTGTGGTTGATGC-3'	Integrated DNA technologies	N/A
Reverse primer for <i>Slc6a4</i> qPCR: 5'-TCAGCCATGTAGCCAAGCACC-3'	Integrated DNA technologies	N/A
Forward primer for <i>Slc7a5</i> qPCR: 5'-CTACGCCTACATGCTGGAGG-3'	Integrated DNA technologies	N/A
Reverse primer for <i>Slc7a5</i> qPCR: 5'-GAGGGCCGAATGATGAGCAG-3'	Integrated DNA technologies	N/A
Forward primer for <i>Slc7a8</i> qPCR: 5'-TCAGCGCCTGTGGTATCATTG-3'	Integrated DNA technologies	N/A
Reverse primer for <i>Slc7a8</i> qPCR: 5'-TGATGCCTGTACGATCCAGA-3'	Integrated DNA technologies	N/A
Forward primer for <i>Tph1</i> qPCR: 5'-AACAAAGACCATTCTCCGAAAG-3'	Integrated DNA technologies	N/A
Reverse primer for <i>Tph1</i> qPCR: 5'-TGTAACAGGCTCACATGATTCTC-3'	Integrated DNA technologies	N/A
Forward primer for <i>VI</i> qPCR (for detection of SARS-CoV-2 viral RNA): 5'-ATGCTGCAATCGTGCTACAA-3'	Integrated DNA technologies	N/A
Reverse primer for <i>VI</i> qPCR (for detection of SARS-CoV-2 viral RNA): 5'-CCTCTGCTCCCTTCTGCGTA-3'	Integrated DNA technologies	N/A
Forward primer for <i>Vil1</i> qPCR: 5'-TCAAAGGCTCTCTCAACATCAC-3'	Integrated DNA technologies	N/A
Reverse primer for <i>Vil1</i> qPCR: 5'-AGCAGTCACCATCGAAGAAGC-3'	Integrated DNA technologies	N/A
Forward primer for <i>VSV-G</i> qPCR: 5'-CAAGTCAAAATGCCAAGATCACA-3'	Integrated DNA technologies	N/A
Reverse primer for <i>VSV-G</i> qPCR: 5'-TTTCCTTGCAATTGTTCTACAGATGG-3'	Integrated DNA technologies	N/A

(Continued on next page)

Continued

REAGENT or RESOURCE	SOURCE	IDENTIFIER
Forward primer for <i>GP</i> qPCR (for detection of LCMV viral RNA): 5'- GCAACTGCTGTGTTCCCGAAAC-3'	Integrated DNA technologies	Peluso et al. ⁸⁶
Forward primer for <i>GP</i> qPCR (for detection of LCMV viral RNA): 5'- CATTACCTGGACTTTGTCAGACTC-3'	Integrated DNA technologies	Peluso et al. ⁸⁶
<i>Ace2</i> Taqman assay	Thermo Scientific	Mm01159006_m1
<i>Doublecortin</i> Taqman assay	Thermo Scientific	Mm00438400_m1
<i>Gapdh</i> Taqman assay	Thermo Scientific	Mm99999915_g1
<i>Maoa</i> Taqman assay	Thermo Scientific	Mm00558004_m1
<i>Vil1</i> Taqman assay	Thermo Scientific	Mm00494146_m1
Software and algorithms		
Agilent software	Agilent	N/A
Bioconductor v.3.8	Bioconductor	https://www.bioconductor.org/
Biorender	Biorender	https://biorender.com/
Flowjo v10.6.2	BD	https://www.flowjo.com/
GSEA	Broad institute	https://www.gsea-msigdb.org/
ImageJ v2.1.0/1.53c	NIH	https://imagej.nih.gov/ij/
Kallisto v.0.46.0	Pachter Lab	https://pachterlab.github.io/kallisto/
Olympic cellSens imaging software	Olympus LS	https://www.olympus-lifescience.com/
Prism v9.3.0	Graphpad	https://graphpad.com
RStudio v.1.2.5019	The R foundation	https://www.r-project.org/
Other		
1% Glycyl-L-tryptophan Diet	Envigo	TD.210749
2" binder clips	Amazon	ASIN B07C94YCR5
Advanced DMEM	Corning	MT10013CV
Amino acid control diet	Envigo	TD.01084
B27 supplement	Gibco	17504044
BioDAQ cages	Research Diets, Inc.	N/A
DAPI mounting media	Electron Microscopy Sciences	17985–50
DNA/RNA Shield Fecal Collection Tubes	Zymo Research	R1137
Elmer's 0.77 oz glue sticks	Amazon	#E517
FBS	Corning	MT35-010-CV
Immulon 4 HBX ELISA plates	Thermo Fisher Scientific	3855
Matrigel (GFR)	BD Biosciences	BD356231
M-MLV Reverse Transcriptase (200 U/ μ L)	Invitrogen	28025013
Neurobasal-A medium	Thermo Fisher Scientific	10888022
Quantitative Synthetic SARA-CoV-2 RNA: ORF, E, N	ATTC	VR-3276SD
Random primers	Invitrogen	48190011
Serum gel tubes	Sarstedt	41.1500.005
Syringe-driven filter units, 0.22 μ m low protein binding durapore membrane	Millipore	SLGVR33RS
Taqman Fast Advanced Master Mix	Thermo Scientific	4444557
TrypLE Express	Thermo Fisher Scientific	12604013
Tryptophan-deficient diet	Envigo	TD.130674
Vacutainer EDTA tubes	BD	365974

RESOURCE AVAILABILITY

Lead contact

Further information and requests for resources and reagents should be directed to and will be fulfilled by the lead contact, Maayan Levy (maayanle@penmedicine.upenn.edu).

Materials availability

Animal strains used in this study are available from The Jackson Laboratory, Taconic Biosciences, or were provided by the indicated investigators.

Data and code availability

- All data and code to understand and assess the conclusions of this research are available in the main text and supplementary materials. RNA-seq data have been deposited and are publicly available. Accession numbers are listed in the [key resources table](#).
- This paper does not contain original code.
- Any additional information required to reanalyze the data reported in this paper is available from the [lead contact](#) upon request.

METHOD DETAILS

Mice

C57BL/6J (000664), TLR3^{-/-} (005217), IFNAR1^{-/-} (028288), K18-HuACE2 (034860), STAT1^{-/-} (012606), Phox2b-Cre (016223), and IDO1^{-/-} (005867) mice were purchased from The Jackson Laboratory. ACE2^{-/-} (18180) mice were purchased from Taconic Biosciences. STAT1^{fl/fl} Villin-cre^{ERT2} mice were obtained by crossing Villin-cre^{ERT2} mice (The Jackson Laboratory 020282) with STAT1^{fl/fl} mice.⁸⁵ At the beginning of each experiment, mice were randomly allocated into experimental groups. In all experiments, age- and sex-matched mice were used. In cases where littermates were not used, mice were cohoused to ensure consistency of common microbiota and genetic background. Mice were 5–12 weeks of age at the beginning of experiments. Both male and female mice were used for experiments, but within each experiment, they were sex matched. Mice were housed at 22.2°C and 52.1% humidity. Mice were given access to food and water *ad libitum* and were maintained under a 12 h light–dark cycle. All mice were maintained in filter-topped cages and given autoclaved food and water at the University of Pennsylvania University Laboratory Animal Resources (Penn ULAR) facility. All experiments were performed in accordance with the guidelines of the respective facilities and were approved by the regulations of the local institutional animal care and use committee (IACUC). No methods were used to predetermine sample size; rather, sample sizes were determined by pilot experiments to assess effect sizes and variability.

Poly(I:C) treatment

Except where noted, mice were intraperitoneally injected with 200 µg of low molecular weight (LMW) poly(I:C) (InvivoGen) once a day for 5 consecutive days, with the last injection occurring 3 h before sacrifice. High molecular weight (HMW) (InvivoGen) poly(I:C) and poly(I:C) from Sigma were also used where noted.

Novel object recognition test

Mice were allowed to acclimate in a rat cage with bedding for 1 h before testing. Following acclimation, mice were allowed to explore an object (glue sticks and 2" binder clips) for 10 min. One hour after exposure to the familiar object, mice were allowed to explore the familiar object and the novel object for 10 min. Novel and familiar objects were randomized between mice. Objects were tested previously to ensure no inherent preference by mice. Interaction was defined as sniffing or direct contact with paws (excluding climbing and chewing behavior). Interaction time with each object was recorded until 30 s of total interaction time was reached. Mice taking longer than 10 min to reach 30 s of total interaction time between the two objects were excluded. The researcher was blinded to treatment groups during testing.

For novel object stimulation prior to sacrifice for hippocampus and NTS analysis, mice were allowed to explore an object (custom made 100 mL glass bottle filled with purple-colored water) for 10 min. One hour after exposure, mice were sacrificed, and brains were fixed for imaging or hippocampus was dissected out and snap frozen in liquid nitrogen and stored at –80°C for downstream analysis.

Radiolabeled tryptophan measurements

Tryptophan extraction and derivatization

Mice were fasted for 36 h before an oral administration of 13C11 L-tryptophan (200 mg/kg body weight). 30 min later, blood was collected via cardiac puncture and serum was snap frozen for downstream analysis. Ileal content was also collected, snap frozen, and weighed. Tryptophan was quantified via ELISA. Percent enrichment of labeled tryptophan was determined as follows: 10 µL of 100 µM norvaline was added to 20 µL of serum. 300 µL of 100% ice-cold acetone was then added to the serum and norvaline mixture and centrifuged at 10,000 x g for 10 min at 4°C. The supernatant containing metabolites was then dried by SpeedVac. The pellet was

resuspended in 100 μ L *N-tert*-Butyldimethylsilyl-*N*-methyltrifluoroacetamide and heated at 70°C for 1.5 h to derivatize. After derivatization, samples were centrifuged at 10,000 \times g for 5 min at room temperature and the supernatant was transferred to a GC-MS vial with a volume reducing insert for analysis.

GC-MS protocol and tracing analysis

1 μ L of sample was injected on splitless mode with an initial temperature of 60°C held for 1 min. The temperature increased at 10°C per minute up to 320°C. Analysis was performed on an Agilent 7890A series GC using a DB-5MS column coupled to a 5975C MSD. Isotopologue abundance was calculated using fluxfix and unlabeled samples from matched tissue. For tryptophan, the 244 *m/z* and 489 *m/z* ions of the 3TBDMS derivative were used for total carbon enrichment. Samples were analyzed up to *m*+11 (489 *m/z* and 244 *m/z*) to account for natural abundance.

In vivo treatments

5-HTP

5-hydroxy-L-tryptophan was administered in drinking water at 1.5 mg/mL for 5 days.

Capsaicin

Capsaicin was dissolved at 25 mg/mL in 10% Tween-80, 10% ethanol, and 80% PBS. 200 μ L of capsaicin was injected intraperitoneally at 2 μ M once daily for 5 days.

Phenelzine

Phenelzine sulfate salt was injected intraperitoneally at 50 mg/kg body weight once daily for 5 days.

680C91

680C91 was dissolved in DMSO and administered via oral gavage at 7.5 mg/kg body weight once daily for 5 days.

Fluoxetine

Fluoxetine oral solution was administered in drinking water at 160 mg/L for 5 weeks.

PCPA

pCPA methyl ester hydrochloride was dissolved in PBS and administered intraperitoneally at 300 mg/kg body weight once daily for 5 days.

m-CPBG

1-(3-Chlorophenyl)biguanide hydrochloride was dissolved in PBS and administered intraperitoneally 10 mg/kg body weight once daily for 5 days.

CNO

Clozapine *N*-oxide hydrochloride was administered intraperitoneally at 2 mg/kg body weight once daily for 5 days.

Tamoxifen

Tamoxifen was dissolved in corn oil and 1 mg of tamoxifen was administered to STAT1^{fl/fl} Villin-cre^{ERT2} mice via oral gavage once daily for 4 consecutive days. Poly(I:C) or vehicle control injections were started one week after the last tamoxifen injection.

Anti-IFNAR1

500 μ g of IFNAR1 blocking antibody was administered intraperitoneally one day before the first poly(I:C) injection (day -1) and at the start of poly(I:C) injections (day 0). 250 μ g of IFNAR1 blocking antibody was then administered on day 1 and day 3 of poly(I:C) injections.

AAV injections

pAAV-hSyn-DIO-hM3Dq-mCherry (Addgene) was administered intravenously at 10¹¹ PFU/mouse to Phox2B-Cre^{-/-} or Phox2B-Cre^{+/-} mice. 2 weeks later, mice were injected with CNO and poly(I:C) once a day for 5 consecutive days.

Patients, participants, and clinical data collection

Acute and recovered cohort

Plasma samples were obtained from a patient cohort previously described.⁸³ Briefly, plasma samples were collected from patients admitted to the Hospital of the University of Pennsylvania with a positive SARS-CoV-2 PCR test between March and May 2020. Recovered donors self-reported a prior SARS-CoV-2 positive PCR test and met the definition of recovered as defined by the Centers for Disease Control and Prevention. Patients with acute SARS-CoV-2 infection were categorized as having moderate or severe disease based on admittance to the intensive care unit (ICU) (moderate patients were not admitted to the ICU, severe patients were hospitalized and admitted to the ICU). This sample collection study was approved by the University of Pennsylvania Institutional Review Board, protocol number 808542. For metabolomics analysis, samples were heat-inactivated at 56°C for 1 h. For serotonin ELISA measurements, samples were not heat-inactivated. Participants provided written informed consent before inclusion in the study.

UPenn PASC cohort

Plasma samples were obtained from 58 patients with PASC seen at the Hospital of the University of Pennsylvania and Presbyterian Hospital. This biosample collection study was approved by the University of Pennsylvania Institutional Review Board, protocol number 849140. Briefly, a blood sample was obtained from each patient and a questionnaire was obtained within 24 h of blood sample collection. For metabolomics analysis, samples were heat-inactivated at 56°C for 1 h. For serotonin ELISA measurements, samples were not heat-inactivated. Participants provided written informed consent before inclusion in the study. Participants were not offered

any monetary compensation for participation. For symptom clustering analysis, questionnaire data from 1,540 individuals was used, UMAP coordinates were calculated, and average symptom levels per cluster were determined.

Viremia cohort

Plasma samples were obtained from a patient cohort previously described.⁸⁴ Briefly, plasma samples were obtained from subjects admitted to the intensive care unit (ICU) with sepsis within 24 h of ICU admission. Source of sepsis was adjudicated by critical care physician investigators. This biosample collection study was approved by the University of Pennsylvania Institutional Review Board, protocol number 808542. Participants provided written informed consent before inclusion in the study.

Healthy cohort

Plasma samples were obtained from healthcare workers in the apheresis unit at the Hospital of the University of Pennsylvania. This biosample collection study was approved by the University of Pennsylvania Institutional Review Board, protocol number 843812. Participants provided written informed consent before inclusion in the study.

UCSF LIINC cohort

Plasma samples were obtained from a patient cohort previously described.¹⁴ Briefly, plasma samples were collected 90–160 days after the first positive SARS-CoV-2 quantitative PCR result. SARS-CoV-2 was not detected in the saliva of these patients at the time of sampling.⁸⁶ Patients were divided into two groups based on symptom assessment at the time of sampling: patients with no COVID-19 attributed symptoms (recovered) and patients with two or more COVID-19 attributed symptoms (PASC). Individuals reporting one COVID-19 attributed symptom were not included.

RUSH PASC cohort

Plasma samples were obtained from a patient cohort previously described.²⁷ Briefly, plasma samples were obtained from individuals with COVID-19 experiencing PASC symptoms 3–4 months after acute COVID-19.

UNCOVER cohort

Plasma samples were obtained from a patient cohort previously described.¹³ Briefly, plasma samples were obtained from individuals who had previously experienced acute COVID-19 at various time points (2–3, 6, 12, 18, and 24 months post-acute infection). Patients with 2 or more symptoms at the time of sample collection were defined as having PASC at that time point. Patients with 0 symptoms at the time of sample collection were defined as recovered. In order to compare the number of PASC symptoms experienced by patients with PASC in the Penn cohort and the UNCOVER cohort, questionnaires were compared and only questions that appeared on both questionnaires were taken into consideration. This totaled to be 26 questions from each questionnaire.

Human tissues

Material from 6 autopsies of patients who died of COVID-19 were obtained from family-consented research-only autopsies performed by the Department of Pathology and Laboratory Medicine at the Hospital of the University of Pennsylvania. Tissues were collected and placed in Trizol and processed for qPCR analysis of total RNA in BSL3 as approved by EHRS. Individuals were then categorized as having died during the acute phase of COVID-19 (within two weeks of the infection) or the post-acute phase of the infection (greater than two weeks after the infection).

Stool samples

Samples were processed as previously described.¹⁷ Healthy donor biosample collection study was approved by the University of Pennsylvania Institutional Review Board, protocol number 833761. Long COVID biosample collection study was approved by the University of Pennsylvania Institutional Review Board, protocol number 849140. Briefly, stool samples were collected in tubes with DNA/RNA shield. Fecal samples were processed within 24 h of receipt by the lab. Upon receipt, samples were homogenized by vortexing for 30 s. Each sample was then aliquoted into cryovials, labeled with the patient ID, and then frozen at -80°C . Samples were thawed and centrifuged at $4000 \times g$ for 10 min at 4°C and the supernatant was sterile filtered through $0.22 \mu\text{m}$ low protein binding durapore membranes. $140 \mu\text{L}$ of the filtered supernatant was transferred to a fresh Eppendorf tube for RNA extraction using the QiaAMP Viral RNA Mini kit. RNA extraction was performed as per manufacturer's protocol and eluted in $60 \mu\text{L}$ of the elution buffer EB from the kit. Extracted RNA was stored at -80°C until further analysis.

Quantification of SARS-CoV-2 viral copies in stool samples

For cDNA synthesis, reverse transcription was performed with random primers and Moloney murine leukemia virus (M-MLV) reverse transcriptase. Synthesized SARS-CoV-2 RNA was used as a standard. Gene-specific primers to SARS-CoV-2 (Wuhan v1, NSP14) and SYBR green master mix were used to amplify viral RNA, and 18S rRNA primers were used to amplify cellular RNA using the QuantStudio 6 Flex RT-PCR system. Copy numbers of viral RNA were calculated using the absolute standard curve method.

Organoids

Tissues from the small intestine were washed with ice-cold PBS, opened longitudinally, and cut into 2 mm pieces. Intestinal pieces were then pipetted up and down three times in ice-cold PBS, and the PBS was then removed. This process was repeated 15–20 times. Crypts were then mechanically separated by shaking in HBSS-EDTA (10 mM) for 15 min and were then filtered through a $70 \mu\text{m}$ strainer into a 50 mL conical tube. Isolated crypts were embedded in Matrigel. Organoids were grown in a modified form of establishment media (described previously)^{87,88} for 3 days and then cultured in differentiation media (described previously)⁸⁹ for two days. Organoids were maintained through passaging by adding ice-cold PBS to the Matrigel plug and digesting with TrypLE Express at 37°C for 2 min. Organoids were treated on day 5 of culture with $20 \mu\text{g}/\text{mL}$ LMW poly(I:C) for 4 h. Organoids

were incubated with 1 ng/mL of recombinant mouse IFN- β 1 or IFN- α for 4 h. To investigate the effects of NF- κ B inhibition, organoids were treated with 1.5 μ M IKK-16 or vehicle control for 2 h prior to poly(I:C) treatment.

Paired food intake and food gavage

Paired food intake

To ensure control and poly(I:C)-treated mice consumed the same amount of food daily, one cage containing 5 mice was given 3 g of food each day. Researcher confirmed that 100% of the food was eaten each day. To avoid competition between cage mates, only female mice were used in paired feeding experiments.

Food gavage

14 g of food (5010 rodent diet) was crushed using a mortar and pestle, passed through a metal sieve, and dissolved in 40 mL of sterile water. The mixture was then filtered through a 70 μ m filter. Mice were given 300 μ L of the food mixture or water via oral gavage, twice a day (morning and evening).

BioDAQ cages

Food intake was measured using BioDAQ food and water monitoring system cages (Research Diets, Inc.). Mice were allowed to acclimate for 3 days before daily injections of poly(I:C).

Platelet depletion

Platelets were depleted using a mixture of purified rat monoclonal antibodies directed against mouse GPIIb α (CD42b). Control mice were injected with a mixture of non-immune rat antibodies (IgG). Mice were injected with 12.5 μ g of antibody intravenously. 24 h post injection, mice were evaluated for serotonin depletion and novel object recognition.

Platelet aggregation FACS

Platelet aggregation was measured as previously described.⁹⁰ Briefly, blood was collected via cardiac puncture into EDTA-coated tubes. Blood was diluted with 2X volume HEPES medium and PRP was collected after a 15-min spin at 50 x g. Platelets were counted and adjusted to equal concentrations between experimental conditions. PRP was divided into two equal portions. One portion was stained with PE-CD9 (1:100) and one portion was stained with APC-CD9 (1:100) for 15 min. Samples were then spun at 2250 x g for 5 min and resuspended in HEPES medium. The two singly stained portions for each sample were mixed 1:1 (volume:volume) before analysis using an LSR flow cytometer. Platelet aggregates were defined as APC⁺ PE⁺ cells.

Western blots

Intestinal epithelial cells were harvested by incubating ileal sections in 3 μ M EDTA and 1.5 μ M DTT on ice for 20 min. Ileal sections were then removed and incubated at 37°C for 10 min in 3 μ M EDTA. Tubes were shaken for 30 s to release epithelium from basement membrane. Remnant tissue was removed, and the epithelial cells were pelleted by centrifugation at 800 x g for 5 min at 4°C. The IEC pellet was resuspended in RIPA buffer [0.1% SDS, 150 mM NaCl, 50 mM tris-HCl (pH 8.0), 0.5% sodium deoxycholate, and 1% NP-40] supplemented with a protease inhibitor cocktail (Sigma-Aldrich). Organoids were harvested by removing media and dissociating the Matrigel plug with ice-cold RIPA buffer. The cells were then centrifugated at 13,000 rpm for 15 min at 4°C, and cell lysates were used to measure protein concentration using the BCA kit. A protein concentration of 20 μ g was then incubated with 5X sample buffer at 100°C for 10 min. Proteins were then separated on 4–15% SDS-polyacrylamide gel electrophoresis gels (Bio-Rad) and transferred to Immobilon-P polyvinylidene difluoride (PVDF) transfer membranes (Millipore). The membranes were blocked with 5% milk in tris-buffered saline with 0.1% Tween 20 (TBST) for 1 h at room temperature and incubated with primary antibodies overnight at 4°C. After three 5-min washes with TBST, the membranes were incubated with horseradish peroxidase (HRP)-conjugated secondary antibodies (1:1000) for 1 h at room temperature. Membranes were then developed with ECL Western blotting reagents (Amersham). The signals were visualized using Amersham Imager 680 (Amersham).

Nodose ganglion extraction, culture, and calcium imaging

Nodose ganglia were extracted and cultured as previously described.^{91,92} Nodose ganglia were collected into Neurobasal-A medium and dissociated in 1 mg/mL collagenase 1A for 1 h at 37°C in serum-free media containing Advanced DMEM, sodium pyruvate solution, and HEPES buffered saline. Nodose ganglion were washed and triturated with glass Pasteur pipettes 60 times and centrifuged 500 x g at 4°C for 5 min. The cell pellet was resuspended into culture media (10% FBS, Neurobasal-A medium, B27 supplement, 50 ng/mL nerve growth factor [NGF], and penicillin/streptomycin) and subsequently seeded onto poly-L-lysine coated (at least 2 h at 37°C, 5% CO₂) 96 well plates and cultured overnight at 37°C, 5% CO₂ incubator. For calcium imaging, the nodose ganglion were washed with fresh serum-free culture media and loaded with 1 μ M Fura-2-AM for 1 h at 37°C. The cells were then washed into modified extracellular Ringer's solution containing 145 mM NaCl, 4.7 mM KCl, 3.4 mM CaCl₂, 1.2 mM KH₂PO₄, 1.2 mM MgSO₄, 1 mM MgCl₂, 10 mM glucose, and 10 mM HEPES. Baseline was measured prior to addition of 50 μ L of either 2 μ M capsaicin or 1 μ M 5-HT, which were directly applied onto neurons. Imaging was conducted immediately in a plate reader at room temperature with wavelengths set to 340, 380, and 510 nm.

Intestinal immunofluorescence

Intestinal sections were fixed overnight in 10% formalin and stored in 70% ethanol before sectioning. Sections were deparaffinized and re-hydrated using serial 5-min incubations in xylene and ethanol gradient (100%–70%). The slides were then washed in PBS and antigen retrieval was performed in citrate buffer (10 mM citrate, pH 6) at 95°C for 1 h. The slides were then washed again in PBS and blocked in 20% normal goat serum and 0.05% Triton X-100 in PBS for 30 min. Sections were incubated with anti-chromogranin A primary antibody at 1:200 overnight at 4°C. Sections were washed with PBS and incubated with goat anti-rabbit AF488 at 1:400 for 2 h at room temperature. Finally, sections were washed and mounted with DAPI mounting media. Images were acquired using a Nikon fluorescence microscope. To quantify chromogranin A positive cells, the number of positive cells were counted in 5, 10x fields and averaged.

Hippocampus and nucleus tractus solitarius (NTS) immunofluorescence

Mice were terminally anesthetized with 2,2,2-Tribromoethanol (Avertin) and perfused with ice-cold PBS and 4% paraformaldehyde (PFA) before decapitation and brain dissection. Brains were then fixed in 4% paraformaldehyde for 4 h at 4°C. For free floating IF sections, brains were cut coronally at 70 μ m using a Leica 1000S Vibratome. Free-floating sections were stained overnight at 4°C in primary antibody in PBS with 0.1% Triton and 1% bovine serum albumin (BSA). The primary antibodies used were cFos (1:1500), Ki67 (1:500), doublecortin (1:500), NeuN (1:500). Sections were washed three times in PBS and incubated with secondary antibodies (1:500) for 1 h at 37°C. After three washes in PBS, the sections were mounted onto charged glass slides and covered with coverslips with Vectashield antifade DAPI aqueous mounting medium. Sections were imaged on a Zeiss LSM 710 confocal microscope with a 10 \times 0.45 NA objective. The entire thickness of the section was imaged at 5 μ m intervals and maximum intensity projections were used for analysis. cFos and Ki67 positive cells were quantified using ImageJ. Each data point is a single mouse.

To quantify doublecortin positive cells, we utilized an artificial neural network (ANN)-based approach. In brief, the network was loosely based on a yolo3 architecture with a total of 120 layers. It contained 79 convolutional layers built with consecutive 3 \times 3 and 1 \times 1 filters followed by a skip connection to help activations propagate through deeper layers without gradients diminishing. The network was entrained by manually providing cell counts of several sets of microscopic images of neurons as a ground truth and accuracy was further improved by giving manual feedback on the ANN-outputs on non-trained datasets.

Metabolomics

For targeted LC/MS metabolomics of amino acids in plasma, 100 μ L aliquots of plasma on ice were spiked with isotopically-labelled amino acid internal standards and extracted with ice-cold methanol according to validated, optimized protocols in a previously published study.⁹³ Extracted amino acids were derivatized using a Waters AccQTag Ultra derivatization kit. Separation and quantitation of derivatized amino acids was achieved using multiple reaction monitoring of calibration solutions and study samples on an Agilent 1290 Infinity UHPLC/6495 triple quadrupole mass spectrometer.^{93,94} Raw data were processed using Mass Hunter quantitative analysis software (Agilent). Calibration curves ($R^2 = 0.99$ or greater) were either fitted with a linear or a quadratic curve with a 1/X or 1/X² weighting.

For the integrative analysis of metabolomics datasets in acute COVID-19, publicly available data were integrated by calculating fold change rates between COVID-19 patients and healthy controls across five studies.^{7–11} Only metabolites detected in at least two studies were considered. Metabolites were then ranked by their average fold change from all five studies.

VSV infections

Vesicular stomatitis virus (Indiana strain) was intravenously administered 2×10^7 PFU. Since VSV does not produce severe infection in C57BL/6 mice, 500 μ g anti-mouse IFNAR-1 antibody was injected intraperitoneally to control and VSV-infected mice, one day before the infection and on the day of the infection. Additionally, 250 μ g of anti-IFNAR-1 was administered 1 day post infection. Mice were sacrificed 24–48 h post infection.

LCMV infections

LCMV Armstrong and LCMV clone 13 were grown in BHK cells (ATCC) and titers calculated by plaque assay as previously described.⁹⁵ For acute infection, mice were injected intraperitoneally with 2×10^5 plaque-forming units of LCMV Armstrong in RPMI supplemented with 1% Fetal Bovine Serum. For chronic infection, mice were injected intravenously with 4×10^6 PFU of LCMV clone 13 in RPMI supplemented with 1% FBS.

Diets

Tryptophan-deficient diet and control amino acid diet were custom ordered from Envigo. Diets were matched for their source of macro- and micronutrient content and differed only in their tryptophan content. Glycine-tryptophan dipeptide diet was custom ordered from Envigo. Glycyl-L-tryptophan hydrate was supplemented in the diet at 10 mg dipeptide/1 g diet on the 5015 diet background (Envigo). Un-supplemented 5015 diet was used as the control diet.

SARS-CoV-2 mouse infections

Virus

SARS-CoV-2 (Isolate USA-WA1/2020) was obtained from BEI Resources (NR-52281) and infectious stocks were grown in Vero-E6 cells (ATCC) and stored at -80°C . SARS-CoV-2 (Isolate B.1.351) for mouse studies was obtained from Andy Pekosz. Infectious stocks were grown in Vero-Ace2-Tmprss2 cells (BEI Resources) and stored at -80°C . All work with infectious virus was performed in a biosafety level 3 laboratory and approved by the Institutional Biosafety Committee and Environmental Health and Safety.

Mouse infections

Animal studies were carried out in accordance with the recommendations in the Guide for the Care and Use of Laboratory Animals of the National Institutes of Health. The protocols were approved by the Institutional Animal Care and Use Committee at the University of Pennsylvania (protocol number 807017). Virus inoculations were performed under anesthesia which was induced and maintained with ketamine hydrochloride and xylazine. Animals were housed in groups and fed standard chow diets. Mice of different ages and both sexes (age and sex-matched within experiments) were administered 1×10^3 or 1×10^5 plaque-forming units (PFU) of SARS-CoV-2 isolate USA-WA1/2020 or isolate B.1.351, respectively, via intranasal administration.

Tryptophan gavage

Mice were fasted for 36 h and then given 200 mg/kg body weight L-tryptophan (dissolved in water at pH 3 and heated at 95°C until complete dissolution) via oral gavage. For analysis of tryptophan levels across time, plasma was collected via cheek bleed before gavage, and 30 and 60 min after.

PTT and aPTT

Blood was collected via cardiac puncture into tubes containing 3.2% trisodium citrate. The final concentration was 9 parts blood and 1 part sodium citrate. Samples were stored at room temperature until centrifugation and were centrifuged at $2000 \times g$ for 10 min at room temperature within 30 min of collection. Plasma was collected and stored at -80°C until analysis. Coagulation testing was done at the IDEXX BioAnalytics N. Grafton, MA Laboratory on 3.2% sodium citrate samples using an STAGO STA Compact Max automated coagulation analyzer.

Flow cytometric assessment of platelet activation

Platelet activation and whole-blood cytometry was performed as described previously,⁹⁶ with a few modifications. Briefly, 200 μL of whole blood was collected via cardiac puncture into tubes containing 25 μL of 3.8% trisodium citrate and 0.4 mM Gly-Pro-Arg-Pro (GPRP). Samples were centrifuged at $350 \times g$ for 10 min at room temperature and 30 μL of the top layer (platelet-rich plasma) was carefully collected with a wide-bore pipette tip and transferred to a separate tube. 120 μL of room temperature PBS^{-/-} was added and samples were centrifuged at $4500 \times g$ for 10 min at room temperature. The supernatant was pipetted off and the platelet pellet was carefully resuspended in FACS buffer containing 0.4 mM GPRP. Half of each sample was stimulated with 0.1 U/mL thrombin at room temperature for 30 min and stained with a 1:100 dilution of rat mAb against mouse P-selectin, labeled with FITC, and a 1:100 dilution of rat mAb against mouse CD41, labeled with APC. Samples were washed with 1 mL of FACS buffer and fixed with 1% PFA on ice for 2 h before analysis using a FACSCanto II flow cytometer.

Hematology analysis

Initial hematology testing for control and poly(I:C)-treated mice was done at the IDEXX BioAnalytics N. Grafton, MA Laboratory. 150 μL of blood was collected via cardiac puncture into tubes containing 15 μL 0.5 M EDTA. Blood samples were kept at room temperature and CBCs were performed within 24 h of collection. Whole blood samples were analyzed using a Sysmex XT-iV automated hematology analyzer with the platelet count also checked by manual blood smear for clumping to ensure sample quality by technicians trained in murine hematology analysis. Subsequent CBCs were performed using The VetScan HM5 (Abaxis). Blood samples were kept at room temperature and CBCs were performed the same day as collection.

Megakaryocyte analysis

Femurs were fixed in 10% formalin for 48 h and then transferred to 20% EDTA (pH 7.4) and kept at 4°C with gentle agitation for 4 weeks. The EDTA solution was changed every 2 weeks. Femurs were then transferred to 70% ethanol, paraffin embedded, sectioned, and stained with hematoxylin and eosin. Evaluation was initially performed blinded to experimental group, with unblinding after evaluation to assist with interpretation of group differences. Megakaryocytes were counted by the number of individual megakaryocytes per single 400x high power field, with sum totals and average given for ten consecutive fields. Whenever possible, evaluation was done within the diaphysis, starting at the most proximal aspect, and extending distally. Using Olympus cellSens imaging software, the glass slides were examined for expedited photomicrographs as well as manual measurement of megakaryocyte diameter. Cells were measured at their widest points.

Platelet and platelet-rich-plasma isolation

Blood was collected via cardiac puncture into Vacutainer EDTA tubes and maintained at room temperature until centrifugation. Samples were centrifuged at $200 \times g$ for 10 min at room temperature. 30 μL of the upper layer of platelet-rich-plasma was added to 120 μL

of PBS^{-/-}. Samples were then centrifuged at 4500 x g at 4°C for 10 min and the upper 120 μL was discarded without disturbing the platelet pellet. Samples were stored at -80°C for downstream analysis.

Metabolite and soluble factor measurements

Samples within experiments were run at the same time, on the same lot number of kits for all ELISA measurements. In cases where less than the required volume was available for individual mice, samples from 2 or more mice from the same experimental group were pooled.

Serotonin

Plasma, isolated platelets, platelet-rich-plasma, and perfused brains were prepared according to manufacturer instructions and serotonin was quantified with Serotonin ELISA kits. Brains were snap frozen in liquid nitrogen and stored at -80°C for downstream analysis. Whole brains were homogenized in PBS^{-/-} and serotonin levels were normalized to total BCA protein.

Tryptophan

Plasma, platelet-rich-plasma, serum, and ileum content were prepared according to manufacturer instructions and tryptophan was measured with Tryptophan ELISA kits. Ileum content was normalized to total weight of the sample.

5-HIAA

Urine was prepared according to the manufacturer instructions and 5-HIAA was measured using 5-HIAA ELISA kits.

Kynurenine

Plasma and livers were prepared according to the manufacturer instructions and kynurenine was measured with Kynurenine ELISA kits. Liver samples were homogenized in PBS^{-/-} and kynurenine levels were normalized to total BCA protein.

Tissue factor

Plasma was prepared according to the manufacturer instructions and tissue factor was measured using Tissue factor ELISA kits.

Fibrinogen

Plasma was prepared according to the manufacturer instructions and fibrinogen was measured using Tissue factor ELISA kits.

TAT complexes

Plasma was prepared according to the manufacturer instructions and Thrombin-antithrombin complexes were measured using Thrombin-Antithrombin Complexes ELISA kits.

BCA protein quantification

Brains and livers were homogenized in PBS^{-/-} and total protein levels were quantified using the Pierce BCA Protein Assay Kit.

RNA sequencing analysis of human organoids

Relative expression of *ACE2* and *SLC6A19* in human small intestinal organoids infected with SARS-CoV-2 was obtained from publicly available RNA sequencing data.³⁰ Briefly, data was analyzed from human intestinal organoids, which were grown in differentiation media and infected with SARS-CoV-2 at a multiplicity of infection (MOI) of 1. Organoids were incubated for 24 h and transcripts from uninfected organoids were compared to infected.

Transcriptional profiling by bulk-RNA sequencing

Libraries were prepared using the Illumina TruSeq stranded mRNA kit with IDT for Illumina TruSeq Unique Dual indexes according to the manufacturer's instructions. Quality and quantity control of RNA and libraries were performed using Agilent 4200 TapeStation and Qubit 4, respectively. Libraries were sequenced on an Illumina NextSeq 550 to produce 75-base pair single-end reads with an average sequencing depth of 7 million reads per sample. Raw reads were mapped to the mouse reference transcriptome (Ensembl; *Mus musculus* version 67) using Kallisto version 0.46.0. Subsequent analysis was carried out using the statistical computing environment R version 3.6.1 in RStudio version 1.2.5019 and Bioconductor version 3.8. Briefly, transcript quantification data were summarized to genes using the tximport package and normalized using the trimmed mean of M values (TMM) method in edgeR. Genes with <1 CPM in $n+1$ of the samples, where n is the size of the smallest group of replicates, were filtered out. Differentially expressed genes were identified with linear modeling using limma (FDR ≤ 0.05 ; absolute logFC ≥ 1) after correcting for multiple testing using Benjamini-Hochberg.

GSEA analysis

Differentially expressed transcripts from RNA-seq on ilea from control or poly(I:C) treated mice were compared to curated gene sets using GSEA software (Broad Institute) with the following parameters; Gene sets database: c5.all.v7.5.1.symbols.gmt [Gene ontology], Number of permutations: 1000, Permutation type: phenotype, Chip platform: Mouse_Gene_Symbol_Remapping_Human_Orthologs_MSigDB.v.7.5.1.chip.^{97,98}

Single-cell RNA-sequencing analysis

Single cell datasets of mouse nodose ganglion was obtained from GEO (Accession number: GSE124312).⁵² Data was analyzed with Seurat v4.⁹⁹ Data was normalized using SCTransform,¹⁰⁰ clustered, and visualized using UMAP. Clusters were annotated and reproduced as described.⁵² Nodose ganglion neurons were subsetted, and expression levels for each gene across all nodose ganglion neurons was visualized using the DotPlot() function in Seurat.

Quantitative real-time PCR

Total RNA from tissues and organoids was extracted using TRIzol and RNAeasy mini kits, respectively. RNA was reversed transcribed using High-Capacity cDNA Reverse Transcription kits. RT-qPCR was performed using QuantiFast SYBR Green PCR kit, New England Biolabs LUNA Universal PCR kit, or Taqman Fast Advanced Master Mix. RT-qPCR was performed on an Applied Biosystems CFX96 machine.

QUANTIFICATION AND STATISTICAL ANALYSIS

Data are presented as means \pm SEM. Replicates represent biologically independent samples. In the figures, asterisks denote statistical significance (* $p < 0.05$, ** $p < 0.01$, *** $p < 0.001$, **** $p < 0.0001$) as assessed by two-tailed Mann-Whitney U test; unpaired two-tailed or one-tailed t test; one-way ANOVA with Tukey's multiple comparisons test, Dunn's multiple comparisons test, Šidák's multiple comparisons test, or Dunnett's multiple comparisons test; Kruskal-Wallis test with Tukey's multiple comparisons test or Dunn's multiple comparisons test; one-tailed linear regression, or hypergeometric test where appropriate. To determine the classification errors of a binary classifier, we calculated the Receiver Operating Characteristics (ROC) and determined the area under the sensitivity/specificity tradeoff curve. UMAP clustering of 1,540 individuals with PASC was performed in R using a matrix of patient records. Statistical analysis was performed in GraphPad PRISM 9 and Microsoft Excel. Graphics were generated in BioRender and Adobe Illustrator.

Supplemental figures

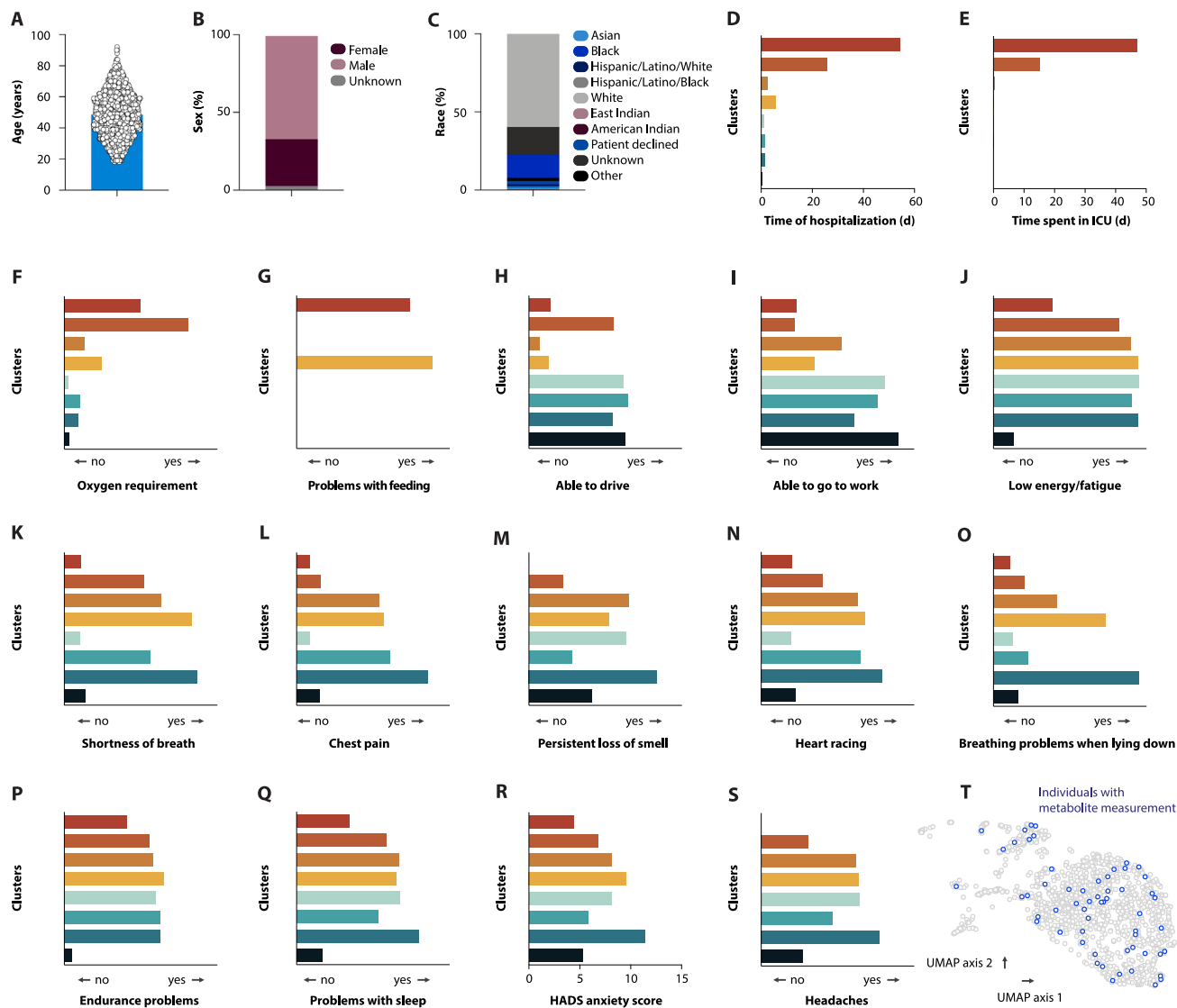


Figure S1. Symptom clusters in a cohort of 1,540 individuals with PASC, related to Figure 1

(A–C) Age (A), sex (B), and race (C) in the UPenn PASC cohort.

(D–S) Symptom distribution in PASC cohort clusters.

(T) UMAP clusters of symptom presentation in UPenn PASC cohort. Highlighted are PASC patients whose circulating metabolite levels were determined.

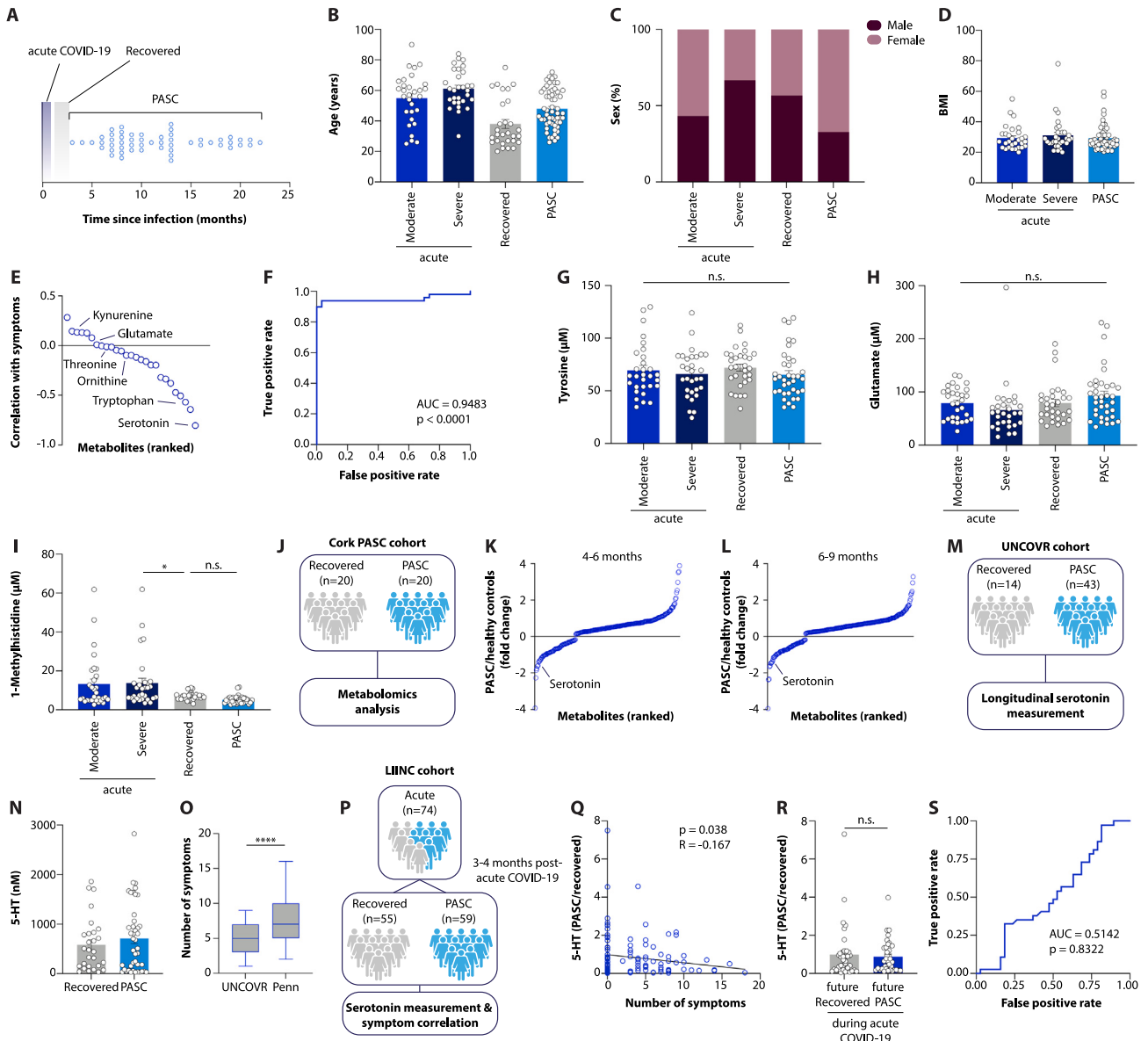


Figure S2. Metabolite changes in PASC, related to Figure 1

(A–D) Time after acute infection (A), age (B), sex (C), and BMI (D) of patients from acute COVID-19, recovered, and PASC cohorts.

(E) Metabolites ranked by their correlation with acute COVID-19 or PASC.

(F) Receiver operating characteristic (ROC) curve of PASC classification based on serotonin measurements.

(G–I) Plasma tyrosine (G), glutamate (H), and 1-methylhistidine (I) levels in acute COVID-19, recovered, and PASC patients.

(J–L) Study schematic (J) and metabolites ranked by differential abundance in PASC compared to healthy controls at 4–6 months (K) and 6–9 months (L) after acute COVID-19 in the Cork PASC cohort.¹²

(M–O) Study schematic (M), serotonin levels of patients recovered from COVID-19 (0 symptoms) and patients with PASC (≥ 2 symptoms) (N), and average symptom number (O) in the UNCOVER cohort.¹³

(P and Q) Study schematic (P) and correlation between the number of PASC symptoms and plasma serotonin level in patients recovered from COVID-19 (symptoms = 0) and patients with PASC (symptoms ≥ 2) 3–4 months following acute COVID-19 (Q) of the UCSF LIINC cohort.¹⁴

(R and S) Serotonin levels during acute COVID-19 in patients who will fully recover versus those who go on to develop PASC (R) and ROC curve of PASC classification based on serotonin levels during acute COVID-19 (S).

Plotted are means \pm SEM or mean \pm min. and max. values (O). n.s. $p > 0.05$, * $p < 0.05$, **** $p < 0.0001$.

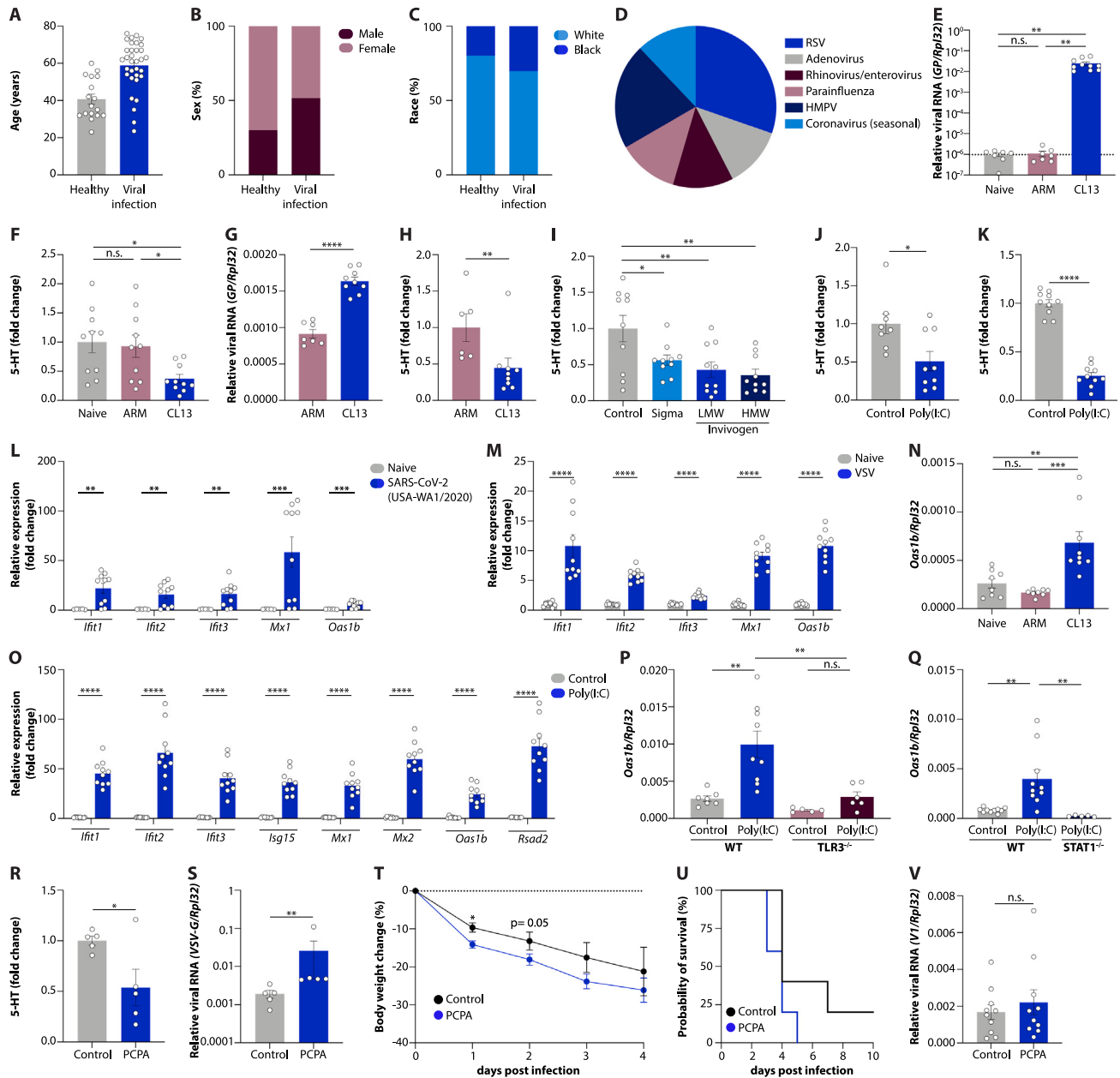


Figure S3. Characteristics of viral inflammation, related to Figure 2

(A–D) Age (A), sex (B), race (C), and source of viral infection (D) of participants with systemic viral infection.

(E–H) Relative viral RNA load in the ileum (E and G) and platelet serotonin levels (F and H) in mice infected with LCMV Armstrong (ARM) or LCMV Clone 13 (CL13) for 30 days (E and F) or 60 days (G and H).

(I) Serotonin levels in mice treated with low-molecular-weight (LMW) or high-molecular-weight (HMW) poly(I:C) from the indicated vendors.

(J and K) Plasma (J) and platelet (K) serotonin levels in mice treated with poly(I:C).

(L–Q) Relative expression of interferon-stimulated genes (ISGs) in lungs of SARS-CoV-2 (USA-WA 1/2020)-infected mice (L); spleens of VSV-infected mice (M); ileum of mice infected with LCMV ARM or LCMV CL13 for 15 days (N); and ileum of poly(I:C)-treated wild-type (O), TLR3^{-/-} (P), and STAT1^{-/-} mice (Q).

(R–U) Platelet serotonin levels (R), viral RNA load (S and V), weight loss (T), and survival curve (U) in PCPA-treated mice infected with VSV for 48 h (S–U) or SARS-CoV-2 (B.1.351) for 7 days (V).

Plotted are means ± SEM. n.s. p > 0.05, *p < 0.05, **p < 0.01, ***p < 0.001, ****p < 0.0001.

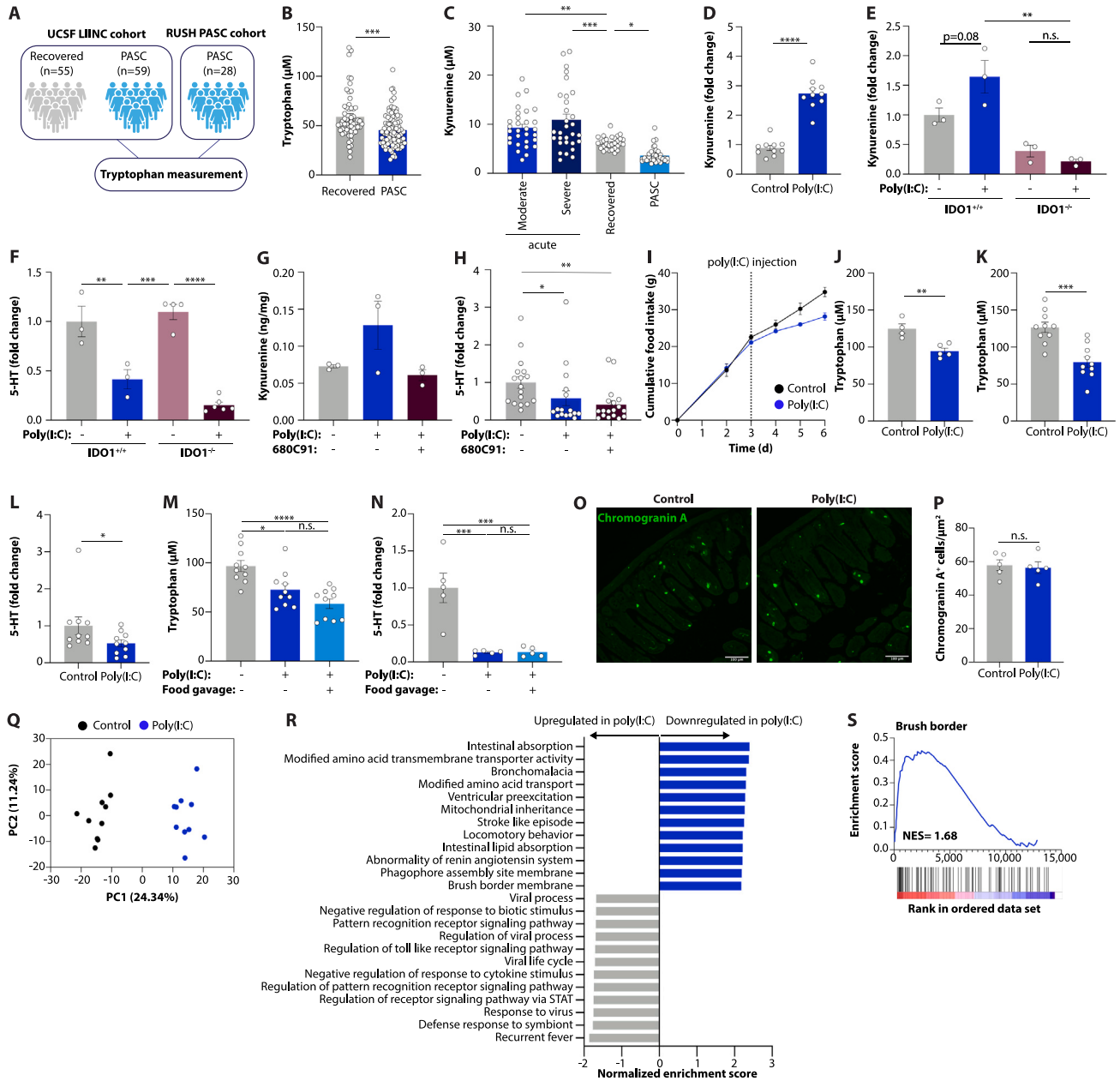


Figure S4. The impact of viral inflammation on metabolite abundances, related to Figure 3

(A and B) Study schematic (A) and plasma tryptophan levels in recovered individuals or PASC patients 3–4 months after acute infection (B) in the UCSF LIINC and RUSH PASC cohorts.^{14,27}

(C and D) Plasma kynurenine levels in acute COVID-19 and after recovery in individuals with PASC (C) and in poly(I:C)-treated mice (D).

(E–H) Plasma kynurenine (E), platelet serotonin (F), liver kynurenine (G), and plasma serotonin (H) in poly(I:C)-treated $\text{IDO1}^{+/+}$ and $\text{IDO1}^{-/-}$ mice (E and F) or mice receiving the TDO2 inhibitor 680C91 (G and H).

(I) Cumulative food intake in mice treated with poly(I:C) or vehicle control. Dotted line indicates the beginning of daily injections.

(J–N) Plasma tryptophan (J, K, and M) and platelet serotonin (L and N) levels in poly(I:C)-treated mice after 36 h of fasting (J), paired feeding with control mice (K and L), or food gavage (M and N).

(O and P) Representative images (O) and quantification (P) of chromogranin A staining in the ileum of poly(I:C)-treated mice. Scale bars, 100 μm .

(Q–S) PCA plot of global gene expression (Q), enriched gene sets (R), and GSEA plot of gene set negatively correlated with poly(I:C) treatment in ileal tissue. Plotted are means \pm SEM. n.s. $p > 0.05$, * $p < 0.05$, ** $p < 0.01$, *** $p < 0.001$, **** $p < 0.0001$.

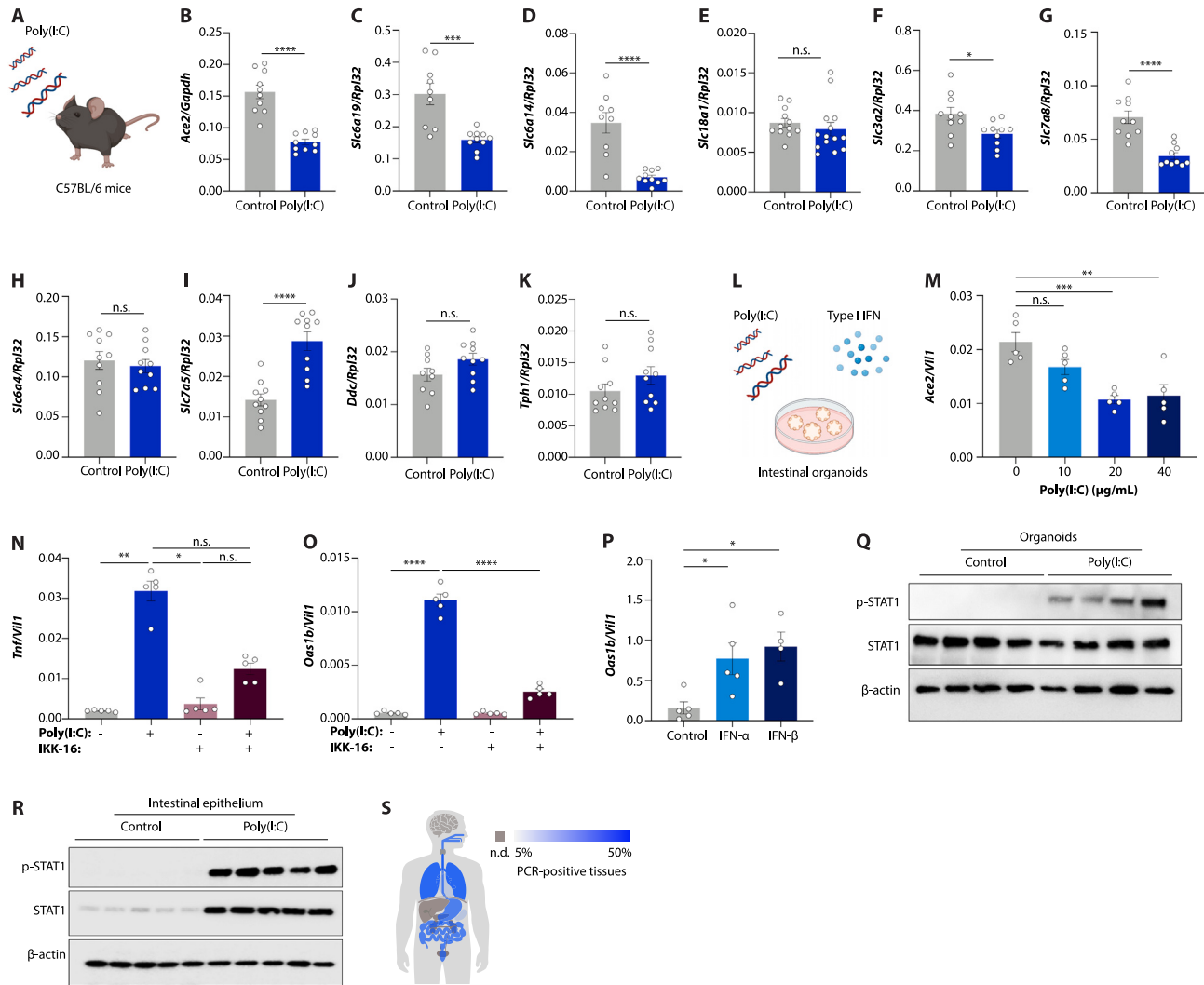


Figure S5. The transcriptional impact of viral inflammation, related to Figure 4

(A) Schematic of the experimental setup for poly(I:C) treatment of mice.

(B–K) qPCR expression of *Ace2* (B), *Slc6a19* (C), *Slc6a14* (D), *Slc18a1* (E), *Slc3a2* (F), *Slc7a8* (G), *Slc6a4* (H), *Slc7a5* (I), *Ddc* (J), and *Tph1* (K) in the ileum of poly(I:C)-treated mice.

(L) Schematic of the experimental setup for treatment of organoids with poly(I:C) or type I IFNs.

(M) *Ace2* expression in murine small intestinal organoids treated with different concentrations of poly(I:C) for 4 h.

(N and O) *Tnf* (N) and *Oas1b* (O) expression levels in small intestinal organoids treated with poly(I:C) and IKK-16.

(P) *Oas1b* expression levels in small intestinal organoids with or without IFN-α and IFN-β.

(Q and R) Western blots of intestinal organoids (Q) or ileal epithelial cells from mice (R) treated with poly(I:C).

(S) Schematic indicating the percentage of SARS-CoV-2 RNA-positive tissues obtained from autopsies >2 weeks after acute infection.

Plotted are means ± SEM. n.s. $p > 0.05$, * $p < 0.05$, ** $p < 0.01$, *** $p < 0.001$, **** $p < 0.0001$.

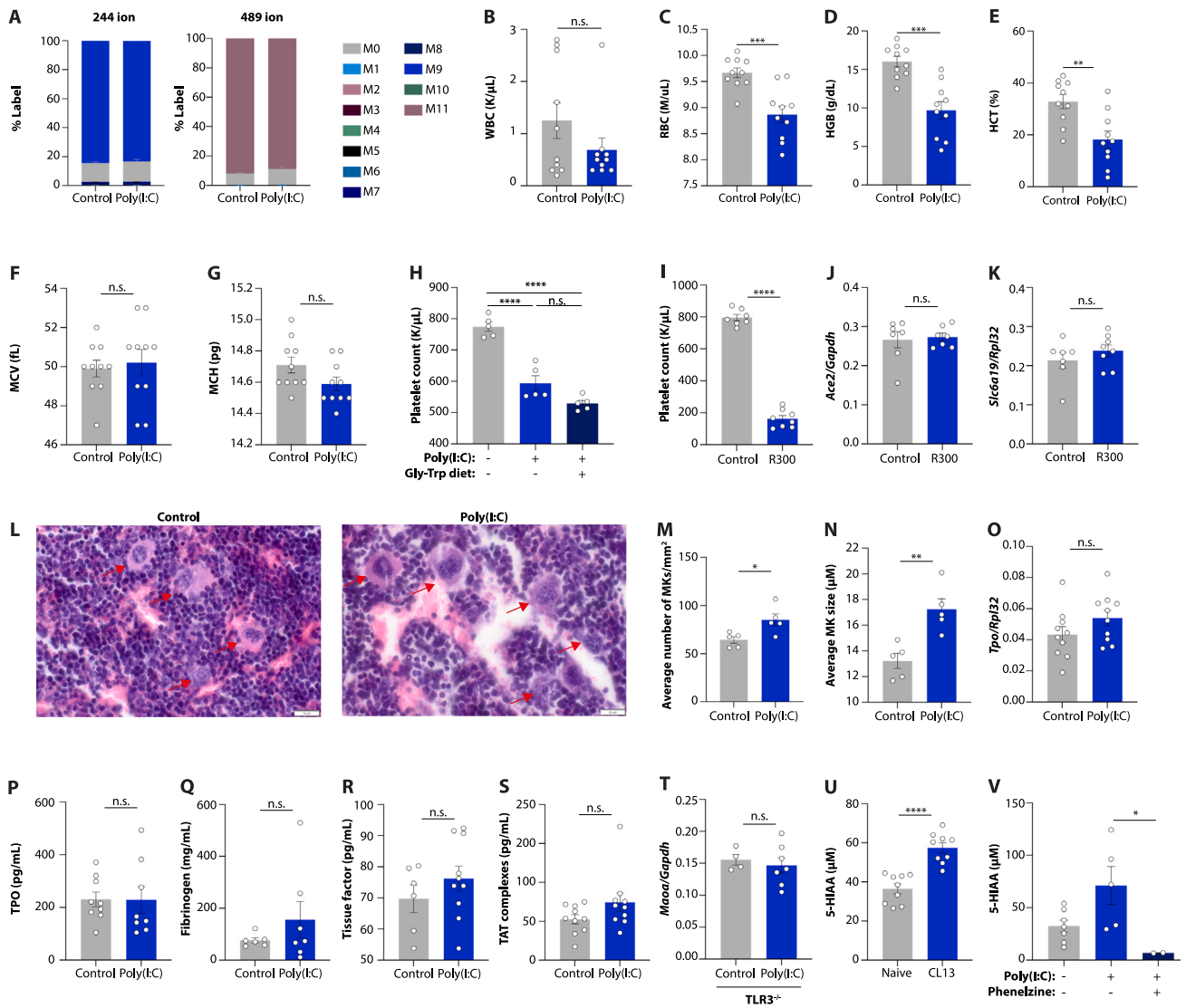


Figure S6. Blood parameters during viral inflammation, related to Figure 6

(A) Fractional labeling of circulating tryptophan after oral gavage in poly(I:C)-treated and control mice. (B–G) White blood cell (WBC) counts (B), red blood cell (RBC) counts (C), hemoglobin (HGB) levels (D), percent hematocrit (HCT) (E), mean corpuscular volume (MCV) (F), and mean corpuscular hemoglobin (MCH) values (G) in poly(I:C)-treated mice. (H) Platelet counts in poly(I:C)-treated mice fed a Gly-Trp dipeptide diet. (I–K) Platelet counts (I), *Ace2* expression (J), and *Sic6a19* expression (K) in mice treated with a platelet-depleting antibody (R300) or isotype control for 24 h. (L–N) Representative images (L) and average number (M) and size (N) of megakaryocytes in femur bone marrow of poly(I:C)-treated mice. Arrows indicate megakaryocytes. Scale bars, 10 μ m. (O) Relative *Tpo* expression in livers of control and poly(I:C)-treated mice. (P–S) Plasma thrombopoietin (TPO) levels (P), plasma fibrinogen (Q), tissue factor (R), and thrombin-antithrombin (TAT) complex (S) in poly(I:C)-treated mice. (T) *Maoa* expression in the ileum of TLR3^{-/-} mice with or without poly(I:C) treatment. (U and V) 5-HIAA levels in urine of mice infected with LCMV CL13 for 30 days (U) and of poly(I:C)-treated mice receiving the MAO inhibitor phenelzine (V). Plotted are means \pm SEM. n.s. $p > 0.05$, * $p < 0.05$, ** $p < 0.01$, *** $p < 0.001$, **** $p < 0.0001$.

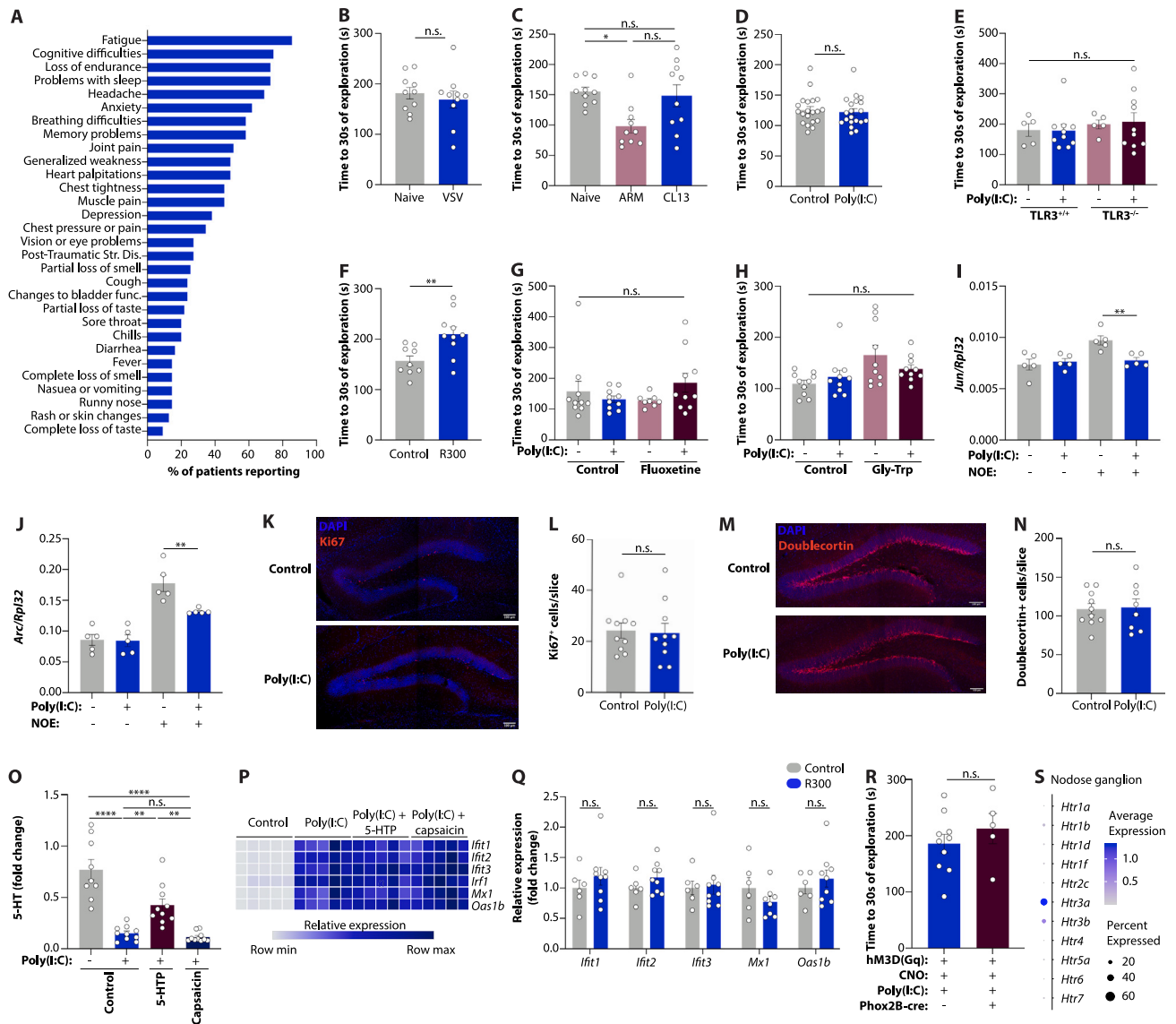


Figure S7. Cognitive performance during viral inflammation, related to Figure 7

(A) Symptoms most commonly reported by patients in the UPenn PASC cohort with targeted metabolomics data.
 (B–H) Total time to reach 30 s of exploration between familiar and novel objects in mice infected with VSV for 24 h (B), mice infected with LCMV ARM or LCMV CL13 for 14 days (C), poly(I:C)-treated mice (D), poly(I:C)-treated TLR3^{-/-} mice (E), mice treated with a platelet-depleting antibody (R300) or isotype control for 24 h (F), poly(I:C)-treated mice treated with fluoxetine (G), and poly(I:C)-treated mice fed a Gly-Trp dipeptide diet (H).
 (I and J) Expression of *Jun* (I) and *Arc* (J) in the hippocampus of poly(I:C)-treated mice with or without NOE.
 (K–N) Representative images (K and M) and quantification (L and N) of Ki67⁺-positive cells (K and L) and doublecortin⁺-positive cells (M and N) in the dentate gyrus of poly(I:C)-treated mice. Scale bars, 100 μ m.
 (O and P) Serotonin levels (O) and relative expression of ISGs in the hippocampus (P) of poly(I:C)-treated mice receiving 5-HTP or capsaicin.
 (Q) Relative expression of ISGs in hippocampi of mice treated with a platelet-depleting antibody (R300) or isotype control for 48 h.
 (R) Total time to reach 30 s of exploration between familiar and novel objects in Phox2b-cre mice injected with AAV-hM3Dq, CNO, and poly(I:C).
 (S) Dot plots of serotonin receptor expression in single-cell RNA-seq data from mouse nodose ganglia.⁵²
 Plotted are means \pm SEM. n.s. $p > 0.05$, * $p < 0.05$, ** $p < 0.01$, *** $p < 0.001$, **** $p < 0.0001$.